

Manuscript Number: MSEA-D-19-00089R2

Title: CAFE based Multi-scale Modelling of Ductile-to-Brittle Transition of Steel with a Temperature Dependent Effective Surface Energy

Article Type: Research Paper

Keywords: Cellular Automata Finite Element (CAFE); Ductile-to-Brittle Transition (DBT); Cleavage; Effective surface energy; TMCR steel

Corresponding Author: Professor zhiliang zhang,

Corresponding Author's Institution: NTNU

First Author: Yang Li

Order of Authors: Yang Li; Shterenlikht Anton; Xiaobo Ren; Jianying He; zhiliang zhang

Abstract: It is still a challenge to numerically achieve the interactive competition between ductile damage and brittle fracture in ductile-to-brittle transition (DBT) region. In addition, since two types of fracture occur at two independent material length scales, it is difficult to process them with the same mesh size by using finite element method. In this study, a framework of modelling DBT of a thermal mechanical controlled-rolling (TMCR) steel is explored by using the cellular automata finite element (CAFE) method. The statistic feature of material's microstructure is incorporated in the modelling. It is found that DBT curve cannot be reproduced with only a temperature dependent flow property, for which another temperature dependent variable must be considered. A temperature dependent effective surface energy based on typical cleavage fracture stage is proposed and obtained through a continuum approach in present work. The DBT of TMCR steel is simulated by using CAFE method implemented with a temperature dependent effective surface energy. It is found that numerical simulation is able to produce a full transition curve, especially with scattered absorbed energies in the transition region represented. It is also observed that simulation results can reproduce a comparable DBT curve contrasting to the experimental results.

1 **CAFE based Multi-scale Modelling of Ductile-to-Brittle Transition of Steel with a**
2 **Temperature Dependent Effective Surface Energy**

3
4 Yang Li¹, Anton Shterenlikht², Xiaobo Ren³, Jianying He¹, Zhiliang Zhang^{1,*}

5 ¹ NTNU Nanomechanical Lab, Department of Structural Engineering, Norwegian University of
6 Science and Technology (NTNU), Richard Brikelands vei 1A, N-7491 Trondheim, Norway

7 ² Department of Mechanical Engineering, University of Bristol, University Walk, Bristol

8 ³ SINTEF Industry, Richard Brikelands vei 2B, N-7465 Trondheim, Norway

9
10 **Abstract:** *It is still a challenge to numerically achieve the interactive competition between ductile*
11 *damage and brittle fracture in ductile-to-brittle transition (DBT) region. In addition, since two types*
12 *of fracture occur at two independent material length scales, it is difficult to process them with the*
13 *same mesh size by using finite element method. In this study, a framework of modelling DBT of a*
14 *thermal mechanical controlled-rolling (TMCR) steel is explored by using the cellular automata finite*
15 *element (CAFE) method. The statistical feature of material's microstructure is incorporated in the*
16 *modelling. It is found that DBT curve cannot be reproduced with only one temperature dependent*
17 *flow property, for which another temperature dependent variable must be considered. A temperature*
18 *dependent effective surface energy based on typical cleavage fracture stage is proposed and obtained*
19 *through a continuum approach in present work. The DBT of TMCR steel is simulated by using CAFE*
20 *method implemented with a temperature dependent effective surface energy. It is found that numerical*
21 *simulation is able to produce a full transition curve, especially with scattered absorbed energies in*
22 *the transition region represented. It is also observed that simulation results can reproduce a*
23 *comparable DBT curve contrasting to the experimental results.*

24 **Keywords:** Cellular Automata Finite Element (CAFE); Ductile-to-Brittle Transition (DBT); Cleavage;
25 Effective surface energy; TMCR steel

26
27
28 **1. Introduction**

29 Ductile-to-brittle transition (DBT) is normally found in the BCC materials, e.g., steel, due to
30 temperature decreasing and loading rate elevation. Ductile fracture usually occurs at higher
31 temperature, e.g. the upper-shelf, with a damage mechanism of void nucleation, growth and
32 coalescence. The well-known Gurson type of model [1-4] and Rousselier model [5] have been widely
33 used to describe ductile fracture accompanying with plastic deformation, in which the critical void
34 volume fraction f_c has been proposed as the failure criterion. While, unstable cleavage fracture is

35 commonly initiated by second-phase particle cracking due to dislocation pile-up, which refers to the
36 sequence of three steps: particle breakage, transgranular fracture within a single grain and overcoming
37 of the grain boundary [6]. A simple model proposed by Ritchie, Knott and Rice [7], so called RKR
38 model, assumes that cleavage failure occurs when the maximum principle stress ahead of the crack tip
39 exceeds the fracture stress σ_f over a characteristic distance. In order to describe the statistical nature
40 of micro-cracks in the stress field, micromechanical models [8-10] following the weakest link
41 philosophy have been reformulated based on RKR model, which provide a promising local approach
42 to understand the essentials of cleavage. One of the most widely used approaches is Beremin model
43 [8], in which a simple expression for macroscopic failure probability can be derived involving a scalar
44 measure of the crack-front loading, the so-called Weibull stress σ_w . Consequently, two main types of
45 the failure criterion for cleavage have been established, critical fracture stress σ_f or Weibull stress σ_w .
46 Whereas, in the DBT regime, two fracture modes coexist, and the final rupture of materials occurs as
47 a consequence of the competition between two failure mechanisms.

48 Modelling of DBT of steel has aroused great interest in past decades. Ductile damage models (e.g.,
49 GTN, Rousselier) combined with RKR criterion model or local approach (e.g. Beremen model) has
50 been widely applied to model the DBT of steel under quasi-static load [11, 12] or dynamic load [13-
51 18]. However, it is basically a post-processing solution to evaluate the occurrence of cleavage after
52 stress field ahead of crack tip obtained from the constitutive equation of ductile model. The
53 competition between two failure mechanisms and the interaction between two failure modes in the
54 transition region are not involved indeed. Furthermore, the fracture in the transition region occurs on
55 two independent scales of microstructure size, ductile fracture related to the spacing of the dominant
56 void initiated from particles, while the brittle fracture related to the grain or cleavage facet size. It is
57 difficult to handle two fracture modes with only one mesh size using the finite element method.
58 Although attempts have been conducted to overcome this problem by using non-local approaches [11,
59 12, 19], it is still a challenge to represent the competition between two failure mechanisms and the
60 interaction between two failure modes in the transition region. However, one approach coupled
61 cellular automata (CA) and finite element (FE), so-called CAFE method, provides a practical solution
62 to solve these two challenges simultaneously [20]. In addition, the statistical feature of microstructure
63 of material can also be represented in this method, e.g. initial void distribution, grain size distribution,
64 misorientation of grain boundaries etc., such that the scatter of toughness in the transition region can be
65 captured. The principle and implementation of CAFE method have been thoroughly described in the
66 ref. [20-25].

67 It is known that the flow properties, e.g., yield stress and strain hardening, will be altered as
68 temperature decreases, which could be a significant factor resulting in the occurrence of DBT.
69 However, only temperature-dependent flow stress is not enough to predict the transition behavior of
70 materials when comparing with the test data reported by Rossoll et al [16], Tanguy et al [18] and

71 Shterenlikht et al [20]. Many efforts have been made to describe temperature dependence of fracture
72 toughness in the DBT transition region. A global approach, Master curve method has been adopted in
73 ASTM E1921 [26], in which the variation of fracture toughness with temperature in DBT region can
74 be described with a reference temperature T_0 . Although the Master curve method is very convenient
75 to apply in practice since only few tests are needed for calibration, it requires high constraint and
76 small scale yielding conditions. Tanguy et al [18] has simulated the DBT of A508 steel with a
77 temperature-dependent σ_u rather than a constant value when modelling the Charpy impact test. By
78 using Master curve method [26] to calibrate the parameters of Beremin model, Petti et al [27],
79 Wasiluk et al [28], Cao et al [29] and Qian et al [30] have also found that σ_u is increasing with
80 temperature in the transition region. Gao et al [31] has found that σ_u increased with temperature
81 reflecting the combined effects of temperature on material flow properties and toughness. Moattari et
82 al[32] accurately predicted the fracture toughness in DBT transition region by introducing a
83 temperature-dependent σ_u described with a summation of athermal and thermally activated stress
84 contribution. A temperature dependent misorientation of grain boundary proposed by Shterenlikht et
85 al [20] has been implemented into the CAFE method to model the DBT of Charpy test of TMCR steel.
86 It has to be noticed that either the temperature dependent σ_u or misorientation proposed in the
87 literature is just a phenomenological parameter for DBT modelling. Therefore, exploring a physical-
88 based variable to disclose the nature of temperature dependent fracture toughness in the transition
89 region is not only significant but also necessary. In this work, on the basis of our previous work [33],
90 a continuum approach is developed to estimate the effective surface energy in the DBT transition
91 region of a TMCR steel. Then, we attempt to establish a framework of numerical prediction of the
92 DBT in steel by utilizing the CAFE method implemented with the temperature dependent effective
93 surface energy.

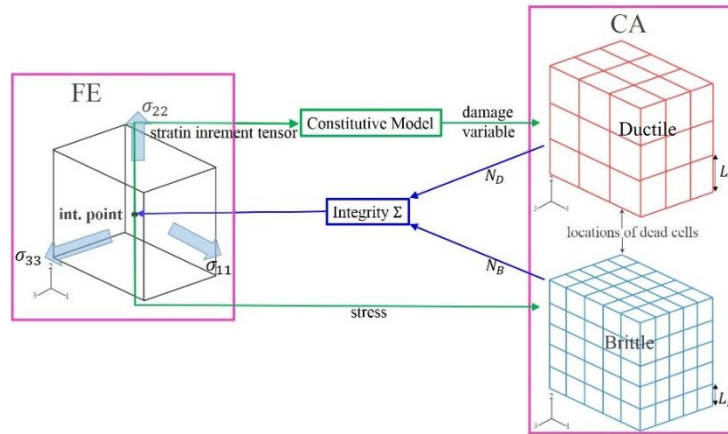
94 The present paper is organized as the followings. Section 2 reviews the CAFE method and discusses
95 the parameters of the model. Section 3 introduces a continuum solution to determine the temperature
96 dependent effective surface energy of TMCR steel. Section 4 describes the finite element procedures
97 and models used to predict the DBT of steels. Section 5 presents the main modelling results of DBT
98 of Charpy tests by using CAFE method implemented with a temperature dependent effective surface
99 energy. The physical nature of the competition between particle size dominated and grain size
100 dominated cleavage propagation is also discussed. The feasibility of CAFE method implemented with
101 temperature dependent effective surface energy is validated by comparing the predicted results to
102 experimental results in the literature [20]. Section 6 ends the paper with a short summary and
103 conclusions.

104

105

1106 **2. The CAFE Method**

1107 The motivation of the CAFE method is to combine the structural and microstructural interactions by
 1108 finite element method [20-22]. The method is divided into two phases: one is finite elements to
 1109 capture the stresses or strains at the structural level, the other is to catch the mechanical essentials of
 1110 the microstructural behavior and its development in a set of CA arrays. Fig.1 shows the
 1111 implementation of the above strategy to deal with the fracture in the transition region where both
 1112 ductile and brittle micro-mechanisms work simultaneously [20]. In each material integration point, the
 1113 microstructure is represented by two CA arrays, where the brittle array represents the cleavage
 1114 behavior while the ductile array processes ductile damage. Structural information, for example,
 1115 stress/strain and damage variable, processed in FE level inputs to CA levels, meanwhile, the
 1116 microstructural evolution and the failure are integrated and send back to the FEs. To achieve the
 1117 implementation of CAFE method in finite element, the explicit dynamic process has been chosen to
 1118 develop a VUMAT by Shterenlikht et al [20-22] so that crack can propagate along a natural failure
 1119 path through element removal.



120
 121 *Fig.1 the illustration of the mechanism of CAFE model in which ductile damage and cleavage*
 122 *fracture have been coupled through two different CA arrays. Here, where N_D and N_B are the number*
 123 *of ‘dead’ cell of ductile CA arrays and brittle CA arrays respectively; Σ is integration indicator; L_D*
 124 *and L_B are the size of cells in brittle and ductile CA arrays.*

125
 126 The Rousellier ductile damage model [5] is adopted to describe the constitutive response at the
 127 integration point. Equation (1) describes the plastic potential of this model

128
$$\frac{\sigma_{eq}}{\rho} - H(\varepsilon_{eq}) + B(\beta)Dexp\left(\frac{\sigma_m}{\rho\sigma_1}\right) = 0 \quad (1)$$

129 where $H(\varepsilon_{eq})$ is the hardening property of material; σ_1 and D are material constants that need to be
 130 tuned; σ_{eq} , σ_m and ε_{eq} are equivalent stress, mean stress and equivalent strain; $B(\beta)$ is the function of
 131 damage variable β ; ρ is relative density, which can be described by

$$\rho = \frac{1}{1 - f_0 + f_0 \exp \beta} \quad (2)$$

132 where f_0 is initial void volume fraction. In ductile CA arrays, cell size L_D is used to characterize the
 133 unit cell size of ductile damage of material with a single void, which normally relates to the spacing of
 134 inclusions or large carbides in steel.

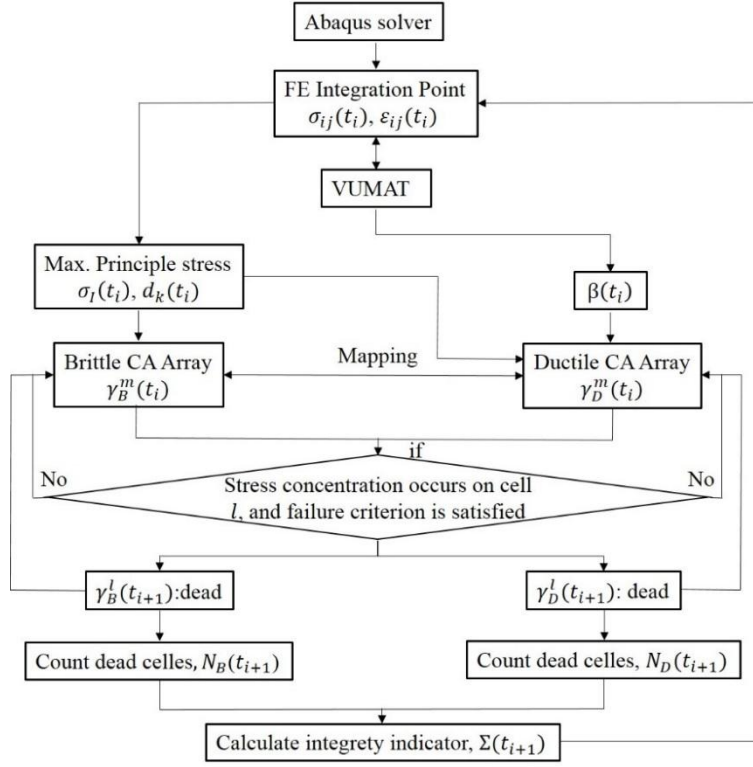
135 According to modified Griffith theory, the critical fracture stress for cleavage can be calculated by

$$\sigma_F = \sqrt{\frac{\pi E \gamma_{eff}}{(1 - \nu^2) d}} \quad (3)$$

136 where γ_{eff} is effective surface energy for the cleavage fracture; E and ν are Young's modulus and
 137 Poisson's ratio respectively; d is grain size. In present work, a temperature dependent effective
 138 surface energy for cleavage will be applied in the CAFE method to calculate critical fracture stress of
 139 cleavage. A fraction of brittle cells, η , in each brittle CA array, is adopted to represent grains with
 140 adjacent grain boundary carbides, where micro-crack has already nucleated. In brittle CA arrays, the
 141 cleavage facet size (d_{CFS}) is applied as the size of cells in brittle CA arrays, e.g. L_B , which can be
 142 measured through fractographic analysis on the fracture surface of specimen [20]. Since the
 143 misorientation between grains is naturally the barrier of cleavage crack propagation crossing the grain
 144 boundary [34], a random orientation is assigned to each cell in brittle CA arrays, and a misorientation
 145 threshold, e.g., θ_{th} , is assumed so that crack can propagate from one cell to the other.

146 The property of CA depends on the state of cells. The state of each cell in next time increment is
 147 determined by its state and the states of neighboring cells at the previous time increment. Once that
 148 the cell is failed due to the fracture propagation, the state of cell will be changed from 'alive', e.g.,
 149 initial state, to 'dead'. Then, the closing neighborhood of 'dead' cell will be stress-concentrated since
 150 the 'dead' cell lost its load-bearing capacity. A framework [22, 25] has described in detail how to
 151 locate such a closing neighborhood around the 'dead' cell. The local concentration factors are utilized
 152 to solve this problem, which are C_D for ductile CA array and C_B for brittle CA array. Thus, at the next
 153 time increment, the states of concentrated cells (either ductile or brittle) are determined by the results
 154 of comparison between the product of damage variable and concentration factors and failure criteria
 155 mentioned above. An integrity indicator, Σ , is used to count the 'dead' cells of both ductile and brittle
 156 CA arrays by which the potential fracture at every current time increment is evaluated. The Σ whose
 157 initial value is 1.0, decreases continuously with the accumulation of damage until N_D or N_B reaches
 158 its maximum value N_{D-max} or N_{B-max} . At this moment, the Σ turns to be zero, which means material
 159 inside the integration point is failed and the integration point does not have loading-bearing capacity
 160 any more. The FE will then be removed from the mesh when the zero Σ is transferred to FE. The Σ
 161 can be calculated by

$$\Sigma = 1 - \max\left(\frac{N_D}{N_{D-max}}, \frac{N_B}{N_{B-max}}\right) \quad (4)$$



162

163 Fig.2 flow chart of the CAFE method. Here, $\sigma_{ij}(t_i)$ and $\varepsilon_{ij}(t_i)$ are stress and strain tensors at time t_i
 164 provided by Abaqus solver; and $\beta(t_i)$ is damage variable of cells given by constitutive model to
 165 ductile CA array at time t_i ; $\sigma_l(t_i)$ is the maximum principle stress of each element calculated from
 166 $\sigma_{ij}(t_i)$; $d_k(t_i)$ is the direction cosines of $\sigma_l(t_i)$; $\gamma_D^m(t_i)$ or $\gamma_B^m(t_i)$ is state of cell m in ductile or
 167 brittle CA arrays t_i ; $\gamma_D^l(t_{i+1})$ or $\gamma_B^l(t_{i+1})$ is state of cell l where stress concentration occurs and
 168 failure criterion is satisfied in ductile or brittle cell arrays at time t_{i+1} ; $N_D(t_{i+1})$ or $N_B(t_{i+1})$ is
 169 numbers of dead cells in ductile or brittle CA arrays at time t_{i+1} ; $\Sigma(t_{i+1})$ is the integrity indicator at
 170 time at time t_{i+1} .

171

172 The calculation process of the CAFE method is presented in Fig.2. It has to be mentioned that in order
 173 to reduce the calculation time, the damage variable $\beta(t_i)$ is given to the ductile CA array instead of
 174 the strain increment tensor $\Delta\varepsilon_{ij}(t_i)$, and accordingly only the solution dependent variable Σ is
 175 returned to the FE from CA array. Both ductile and brittle CA arrays are used only for the simulation
 176 of fracture propagation at each CA scale, while, the constitutive response is calculated at FE level. In
 177 addition, for the easy achievement of convergence, in ductile CA array a normal distribution of
 178 damage value β_F rather than that of f_0 is adopted. At each increment of deformation, the model
 179 compares the present damage variable β with the failure value β_F until the material failed. Since two

180 CA arrays occupy the same physical space, the evaluation of the cells shall be synchronized in both
 181 CA arrays. Thus, a mapping rule has been introduced in the CAFE method to reflect dead cells in
 182 ductile CA array into the corresponding brittle CA array, and vice versa [21]. After stress
 183 concentration occurred on the cell m in either CA arrays, it becomes dead when failure criteria are
 184 satisfied. A more detailed description about the CAFE method can be found in literature [21].

185

186

187 **3. The Temperature dependent effective surface energy**

188 Based on the theory of shielding effect of dislocation mobility on crack tip, a method has been
 189 proposed [33] to predict the temperature dependent effective surface energy of single-crystal iron in
 190 the ductile-to-brittle transition (DBT) region. In the present work, this method will be extended to
 191 calculate the effective surface energy of steel in the transition region.

192 The shielding effect of the dynamics of dislocation on crack tip stress field can be assessed with a
 193 continuum method [33, 35, 36]. It is assumed that the material is isotropic, and that the rate-dependent
 194 plastic deformation is induced by dislocation emission and motion. According to Orowan law, the
 195 shear strain rate, $\dot{\gamma}^p$, can be used to describe the plasticity caused by the dislocation mobility

$$\dot{\gamma}^p = \alpha \rho_d b v \quad (5)$$

196 Where α is a proportionality constant; ρ_d is the dislocation density; b is Burgers vector; v is
 197 dislocation velocity. The dislocation velocity v can be obtained from the function of resolved shear
 198 stress τ and temperature Θ , e.g., the empirical Arrhenius type law

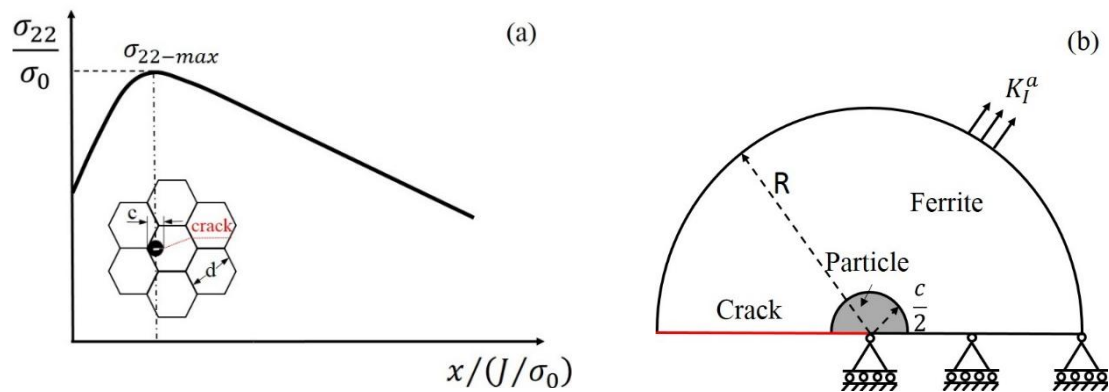
$$v = v_0 \exp\left(-\frac{Q}{k_B \Theta}\right) \left(\frac{\tau}{\tau_0}\right)^m \quad (6)$$

199 where Q is the activation energy for dislocation velocity; k_B is the Boltzmann constant; m is a
 200 material constant for wide range of stress level; v_0 is material specific reference dislocation velocity;
 201 τ_0 is normalization shear stress; here Θ is the absolute temperature in Kelvin. Since the material is
 202 assumed to be isotropic, the von Mises equivalent stress σ_{Mis} and the equivalent plastic strain
 203 rate $\dot{\epsilon}^p$ can be used to replace the plastic shear strain rate $\dot{\gamma}^p$ in equation (5) and the resolved shear
 204 stress τ in equation (6). Then, after inserting the equation (6) into equation (5), the equivalent plastic
 205 strain rate $\dot{\epsilon}$ to describe the rate-dependent plasticity induced by the dislocation mobility can be
 206 derived

$$\dot{\epsilon} = \dot{\epsilon}_0 \exp\left(-\frac{Q}{k_B \Theta}\right) \left(\frac{\sigma_{Mis}}{\sigma_0}\right)^m \quad (7)$$

207 where $\dot{\epsilon}_0$ is a reference strain rate; σ_0 is a normalization stress.

208 It is known that DBT normally occurs in body centered cubic (BCC) metals, e.g., single-crystal iron,
 209 Fe alloys and steel, due to the thermal-activated dislocation emission and motion [37]. The difference
 210 between single-crystal iron and steel is the presence of impurities (e.g., particles), grain boundary and
 211 preexisting dislocations in the latter, which affects the dislocation behavior, for instance, nucleation,
 212 motion, multiplication etc. If their effect on the fracture of the latter can be described by the change of
 213 dislocation density near crack tip comparing with that of former, see equation (5), the model
 214 developed for single-crystal iron is possible to be applied to the steel according to the theory of the of
 215 shielding effect of dislocation mobility on crack tip. To do this, several assumptions have to be made.
 216 Firstly, a micro-crack is assumed to be initiated within a grain boundary particle, e.g., carbide or
 217 inclusion, at a position x_c ahead of the notch/crack tip where the local tensile stress equals to the
 218 maximum principle stress, see Fig.3 (a). Then, the nucleated micro-crack will penetrate the interface
 219 between particle and matrix once that local tensile stress at interface exceeds the fracture stress.
 220 Secondly, we postulate that the penetration of the micro-crack into the interface leads to the final
 221 unstable cleavage fracture, namely the crack resistance of grain boundary is not taken into account.
 222 Further, it is assumed that the crack penetration from particle into matrix is dominated by a local K -
 223 field. Then, the elastic zone (dislocation free zone) in the continuum model for single-crystal material
 224 [33] is replaced with an elastic particle, and the viscoplastic material outside the elastic region is
 225 defined as the ferrite, e.g., a time-dependent plastic matrix. Thus, a new continuum model can be
 226 adopted to estimate the fracture toughness of steel in the transition region, see Fig.3 (b).



227
 228 *Fig.3 the continuum model: (a) the schematic illustration of the micro-crack initiation and*
 229 *propagation across the interface and grain boundary, c is the particle diameter, and d is grain size;*
 230 *(b) MBL model to calculate the effective surface energy for cleavage extension across the interface*
 231 *between particle and matrix [33]. c is particle size.*

232
 233 Only the upper-half of model is presented due to symmetry, see Fig.3 (b). A small circle around the
 234 crack tip with a radius $c/2$ is the elastic zone, e.g., particle. The radius of model R is 20 times larger
 235 than the elastic zone size. Outside the elastic zone, there is the matrix, e.g., ferrite, which is time-

236 dependent plastic material described by the equation (7). A crack with an initial radius of $1.15 \times$
 237 $10^{-4}R$ is located in the center of model. Abaqus 6.14 is employed, and 4-node and plane strain
 238 elements (CPE4) are used in all simulations. Through the nodal displacement on the outer boundary
 239 layer in the MBL model, a linear elastic K_I field, e.g., the applied stress intensity factor K_I^a , with a
 240 constant loading rate \dot{K} is implemented. To calculate the effective surface energy, only a stationary
 241 crack is studied.

242 For a sharp crack tip, cleavage fracture occurs once the crack tip stress intensity factor equals to the
 243 critical value, i.e. $K_I^t = K_{IC}$. The critical stress intensity factor K_{IC} depends only on the material's
 244 surface energy γ_s in terms of the Griffith criterion. Due to the shielding effect of plastic deformation
 245 on the crack tip stress field, the local stress intensity factor K_I^t at crack tip is always lower than the
 246 applied stress intensity factor K_I^a , particularly at higher temperature. The applied stress intensity
 247 factor K_I^a at the moment of failure, e.g. $K_I^t = K_{IC}$ is regarded as the fracture toughness of material.
 248 According to modified Griffith theory, $G_c = 2(\gamma_s + \gamma_p)$, if let $\gamma_s + \gamma_p = \gamma_{eff}$, the effective surface
 249 energy can be obtained by

$$\gamma_{eff} = \frac{(1 - \nu^2)}{2E} K^2 \quad (8)$$

250 Thus, the applied stress intensity factor K_I^a at cleavage fracture can be calculated, and
 251 accordingly the effective surface energy for cleavage extension across the particle-matrix
 252 interface of steel in the transition region can also be obtained from equation (8).

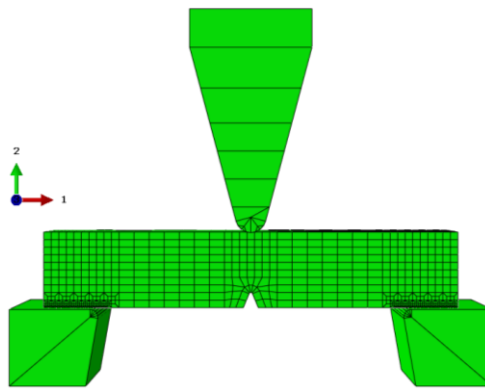
253

254

255 **4. Numerical simulation**

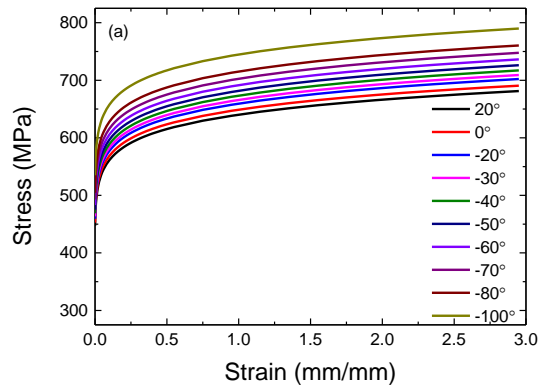
256 An explicit dynamic process is adopted to model the Charpy test by using an explicit code with CAFE
 257 strategy implemented, which has been introduced in Section 2. The geometry of Charpy V-notch
 258 specimen is 55mm*10mm*10mm according to the standard ASTM E23 16b [38], the notch radius
 259 and notch depth are 0.25mm and 2.0mm respectively. The striker and anvils size and geometry are
 260 also those of the standard ASTM E23 16b [38]. The finite element model of Charpy test is shown in
 261 Fig.4, in which the full Charpy specimen is meshed with 8 nodes and reduced integration elements
 262 (C3D8R). Cells are assembled only to those elements in a small region in the center of specimen with
 263 a mesh size around 1mm, so-called damage zone, where damages in a real Charpy specimen is
 264 expected. The striker and two anvils are modelled as elastic body, and are meshed with C3D8R and
 265 C3D6 type of elements. The total number of elements in this model is 8250, in which damage zone
 266 composes of 700 elements. The contact between the Charpy specimen and striker and anvils is
 267 modeled with a friction coefficient 0.15. The initial velocity of striker is 5.5 m/s.

268 It is assumed that L_D and L_B are $200\mu m$ and $100\mu m$ respectively. Then, in the ductile CA arrays,
 269 each cubic array has 5 cells per linear dimension, namely $m_D = 5$. Likewise, in the brittle CA arrays,
 270 each cubic has 10 cells per linear dimension, namely $m_B = 10$. Therefore, in each element or
 271 integration point, there are 125 ductile cells and 1000 brittle cells. Accordingly, the damage zone is
 272 composed of 87500 ductile cells and 700000 brittle cells. It is assumed that the CA array either ductile
 273 or brittle loses the load-bearing capacity when the cells in one orthogonal section of CA array are
 274 failed [21]. Therefore, the maximum numbers of the dead cells in each CA array are taken as
 275 $N_{D-max} = m_D^2 = 25$ for ductile CA array and $N_{B-max} = m_B^2 = 100$ for the brittle CA array. The
 276 concentration factor for ductile CA, e.g., C_D , is 1.4 and that for brittle CA, e.g., C_B , is 1.4 and 11.0
 277 respectively [20].



278
 279 Fig.4 Finite element model of the Charpy test.

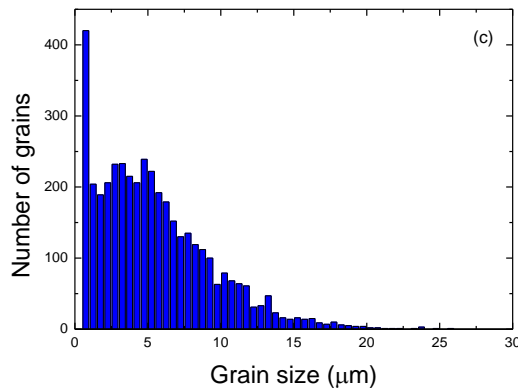
280
 281 The initial void volume fraction f_0 is assumed to be 0.0001. The statistical feature of damage failure
 282 value β_F conforms to a normal distribution, in which the mean value β_{F-mean} is 8.0 and the standard
 283 deviation β_{F-std} is 1.2. The material constant D and σ_1 are 1.65 and 400MPa respectively. These
 284 values of ductile damage variables used in the present work has been calibrated with experimental
 285 results of pure ductile fracture, for example the upper shelf energy (USE) of Charpy test. The flow
 286 property of the TMCR steel at different temperature is presented in Fig.5 (a). The microstructure of
 287 this TMCR steel is presented in the Fig.5 (b), which consists mainly of ferrite and some banded
 288 pearlites. Based on the measurement of grain size of this TMCR steel, the histogram of grain size
 289 distribution is obtained as shown in the Fig.5 (c), which presents a bimodal distribution. Since these
 290 tiny grains will never fracture as they have very high fracture strength, the modelling results are not
 291 affected by omitting this small volume of tiny grains. Hence, an equivalent unimodal three-parameter
 292 Weibull distribution is applied to characterize the grain size distribution of this material, in which the
 293 scale, shape and location parameter are 1.223, 5.392 and 0.516 respectively. The fraction of brittle CA
 294 cells that cleavage is nucleated, η , is assumed to be 0.01, which has been adopted by Shterenlikht et al
 295 [20] as well. The misorientation threshold θ_{th} is assumed to be 40° . The effective surface energy for
 296 the fracture stress of cleavage will be calculated in the section 5.



297



298



299

300 *Fig. 5 The properties and microstructure of TMCr steel: (a) flow stress and strain curve at different*
 301 *test temperatures[21], (b) the microstructure of TMCr steel [20] and (c) the histogram of grain size*
 302 *distribution [20].*

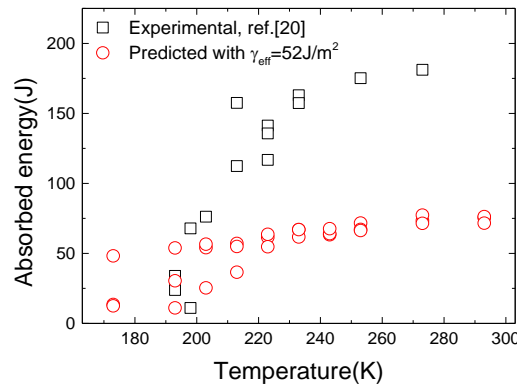
303

304

305 **5. Numerical results and discussion**

306 In the following, we firstly present the predicted results of DBT by using a constant effective surface
 307 energy. To reproduce the transition by using the CAFE method, another temperature dependent
 308 variable, e.g., the temperature dependent effective surface energy, is calculated via the continuum
 309 approach introduced in the Section 3. Although being improved, the DBT predicted with the
 310 calculated temperature dependent effective surface energy indicates that the role of grain boundary in
 311 the cleavage propagation in the transition region cannot be neglected. As such, the lower limit of

312 effective surface energy for overcoming the barrier of grain boundary in the transition region is
 313 estimated based on both the temperature dependent effective surface energy for unstable cleavage
 314 formation and the size ratio of cleavage facet (unit) to critical particle. In the end, an accurate
 315 prediction of DBT of TMCR steel is achieved by using the lower limit of effective surface energy for
 316 crack propagating across the grain boundary.



317

318 *Fig.6 absorbed energy of Charpy impact test in the transition region predicted by CAFE model with a*
 319 *constant effective surface energy, e.g., $\gamma_{eff} = 52 J/m^2$.*

320

321 **5.1 DBT prediction by using a constant effective surface energy**

322 Firstly, a constant value of the effective surface energy γ_{eff} , $52 J/m^2$, which has been adopted in the
 323 study on the DBT of TMCR steel by Wu et al [23] and Shterenlikht et al [20], is used in the CAFE
 324 model to calculate the fracture stress of cleavage according to equation (3). The other parameters to
 325 model the DBT of TMCR steel have been introduced in the Section 4. The absorbed energy of
 326 standard Charpy tests in the transition region vs. temperature is plotted in the Fig.6, in which the
 327 predicted results by CAFE method with constant effective surface energy compare with the
 328 experimental results by Shterenlikht et al [20]. At each temperature, three runs have been performed.
 329 Since the statistical nature of material has been incorporated in the model, results present a scattered
 330 feature as shown in the Fig.6. It can be found that the predicted absorbed energy at higher temperature
 331 is not as scattered as that at lower temperature since the fewer cleavage happens at higher temperature.
 332 The predicted absorbed energy at lower temperature, e.g., 193K, is comparable to the experimental
 333 results. However, the predicted absorbed energy is dramatically underestimated comparing to the
 334 experimental results. It implies that only temperature-dependent flow stress of material shown in Fig.5
 335 (a) is not adequate to obtain an ideal DBT behavior, which has been similarly reported by Rossoll et al
 336 [16], Tanguy et al [18] and Shterenlikht et al [20]. Thus, the second temperature-dependent parameter
 337 has to be searched so as to accurately represent the DBT behavior of materials.

338

339 **5.2 The effective surface energy of TMCR steel**

340 5.2.1 Identification of the parameters

341 It is found that the variation of activation energy of DBT among single-crystal iron, poly-crystal iron
 342 and Fe-alloys is relatively minor [39, 40], e.g., in the range of 0.2-0.5. This implies that the minor
 343 difference between parameters calibrated from the activation energies of DBT of different steels can
 344 be expected. In addition, there are still some resemblances between low carbon steel studied by
 345 Tanaka et al [40] and the TMCR steel investigated in the present work, e.g., the ferritic type of
 346 microstructure and controlled-rolling process of production. Since the absence of the test results of
 347 activation energy of DBT of the TMCR steel, a low carbon steel experimentally obtained by Tanaka
 348 et al [40] is utilized to approximately identify the parameters for the calculation of effective surface
 349 energy of the TMCR steel. In the aim of exploring a solution to estimate the effective surface energy
 350 in transition region, the gap between two materials, e.g., low carbon steel and the TMCR steel can be
 351 ignored.

352 As reported in the literature, a relation between loading rate \dot{K} and Θ_c has been found through
 353 experiments [41]

$$\ln \dot{K} = -E_a/k_B \Theta_c + const. \quad (9)$$

354 where E_a is the activation energy for the DBT, which equals to the activation energy Q for dislocation
 355 velocity; Θ_c is critical DBT temperature at which ductile fracture changes to be brittle fracture [33, 35,
 356 36]. Based on the theory of shielding effect of dislocation mobility on crack tip, equation (9) has also
 357 been used to depict the correlation of loading rate and Θ_c of low carbon steel by Tanaka et al [40].
 358 The critical transition temperatures of low carbon steel have been measured through four point
 359 bending tests under different outer-fiber strain rates by Tanaka et al [40]. The outer-fiber strain rate
 360 can be calculated by [42]

$$\dot{\epsilon}_f = \frac{4B}{S_1^2} \dot{\delta} \quad (10)$$

361 where $\dot{\epsilon}_f$ is the outer-fiber strain rate and $\dot{\delta}$ is the cross head speed, B is the thickness of specimen and
 362 S_1 is the outer span of specimen. The applied stress intensity factor of four point bending test can be
 363 calculated by using the equation [43]

$$K_I = \frac{3F(S_1 - S_2)}{2BW^2} \sqrt{a} Y \quad (11)$$

364 where $Y = \frac{1.1215\sqrt{\pi}}{(1-a/W)^{3/2}} \left[\frac{5}{8} - \frac{5}{12} \frac{a}{W} + \frac{1}{8} \left(\frac{a}{W} \right)^2 + 5 \left(\frac{a}{W} \right)^2 \left(1 - \frac{a}{W} \right)^6 + \frac{3}{8} \exp \left(-6.1342 \frac{a}{W-a} \right) \right]$, F is loading
 365 force, S_2 is inner span, W is width of specimen and a is notch depth. To obtain the loading rate of
 366 four point bending test, three-dimensional analysis with a quasi-static process is carried out in the
 367 present study. The cross head speed applied for modelling is converted from outer-fiber strain rates
 368 used by Tanaka et al. [40] in terms of the equation (10). It has to be mentioned that only a stationary

369 crack is studied. The Young's modulus E and poisson's ratio ν of steel are 206 GPa and 0.29
 370 respectively. The loading rate, e.g., the rates of stress intensity factor, applied on the four-point
 371 bending specimen is calculated by equation (11). The outer-fiber strain rates and calculated loading
 372 rate, e.g., the applied rates of stress intensity factor are listed in table 1.

373 Tab.1 The outer-fiber strain rates of the four point bend tests on fully annealed low carbon steel [43]
 374 and the calculated applied rates of stress intensity factor.

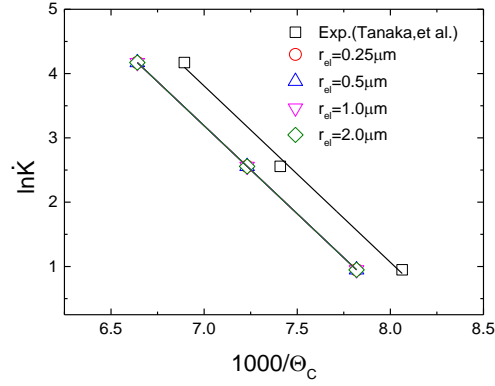
$\dot{\epsilon}(s^{-1})$	$\dot{K}_I^a(MPam^{0.5}s^{-1})$
4.46e-4	2.5790
2.23e-4	12.897
1.12e-2	64.774

375

376 The critical DBT temperature under a specific loading rate can be predicted by using the continuum
 377 approach introduced in section 3. Different elastic zone size (e.g., particle size) of the model is also
 378 studied. To obtain the critical DBT temperatures under the loading rates listed in table 1, for each
 379 elastic zone size, several groups of parameters have been tried following the method introduced
 380 previously by the authors [33]. By doing this, groups of parameters are optimized for each elastic
 381 zone size, which are listed in the table 2. The computed DBT temperatures under different loading
 382 rates are compared with experimental results by Tanaka et al [40] in Fig.7. It is shown that the
 383 computational results of low carbon steel agree well with experimental results, which indicates that
 384 the group of parameters for each elastic zone size is reliable. Meanwhile, the influence of the elastic
 385 zone size on the fracture toughness in the transition region is also studied under the loading rate 10
 386 $MPam^{0.5}s^{-1}$. The applied stress intensity factor K_I^a normalized with the critical stress intensity factor
 387 K_{IC} vs. temperature are plotted in the Fig.8 for each elastic zone size. Here, $K_{IC} = 1.77MPam^{0.5}$ is
 388 calculated from the widely used effective surface energy for cleavage of steel, e.g., $7J/m^2$, tested by
 389 Bowen et al [44] according to Griffith theory. It is shown in Fig.8 that to achieve an identical DBT
 390 temperature Θ_c the minor difference among the fracture toughness for different elastic zone sizes is
 391 presented in the whole temperature range by using the parameters identified above. Recall the
 392 equation (5)-(7), at a specific temperature and under same stress level, when activation energy Q is
 393 determined, with the combination of parameter of $\dot{\epsilon}_0$ and m , the similar amount of shielding effect of
 394 dislocation dynamics and DBT behavior can be always achieved no matter how large the elastic zone
 395 size (particle size) is. To this end, it can be concluded that the predicted DBT of low carbon steel by
 396 using the continuum model is elastic zone size independent. In the later simulation, the parameters
 397 verified for elastic zone size $1\ \mu m$ will be adopted.

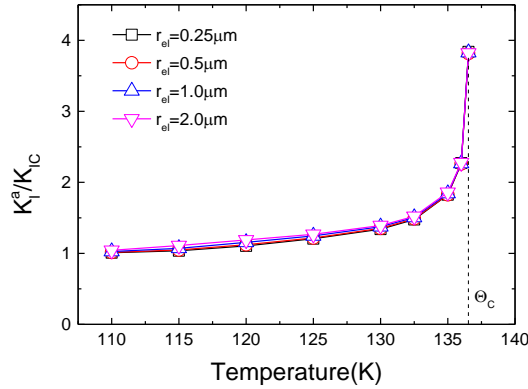
398 Tab.2 Parameters for different elastic zone size.

$r_{el}(\mu m)$	$\dot{\epsilon}_0(s^{-1})$	$Q(ev)$	m	σ_0
0.25	29934.39	0.236	1.45	1.0
0.50	11307.01	0.236	1.70	1.0
1.0	3898.48	0.236	2.00	1.0
2.0	1717.67	0.236	2.30	1.0



399

400 *Fig.7 comparison of computed and experimental critical DBT temperature of low-carbon steel.*



401

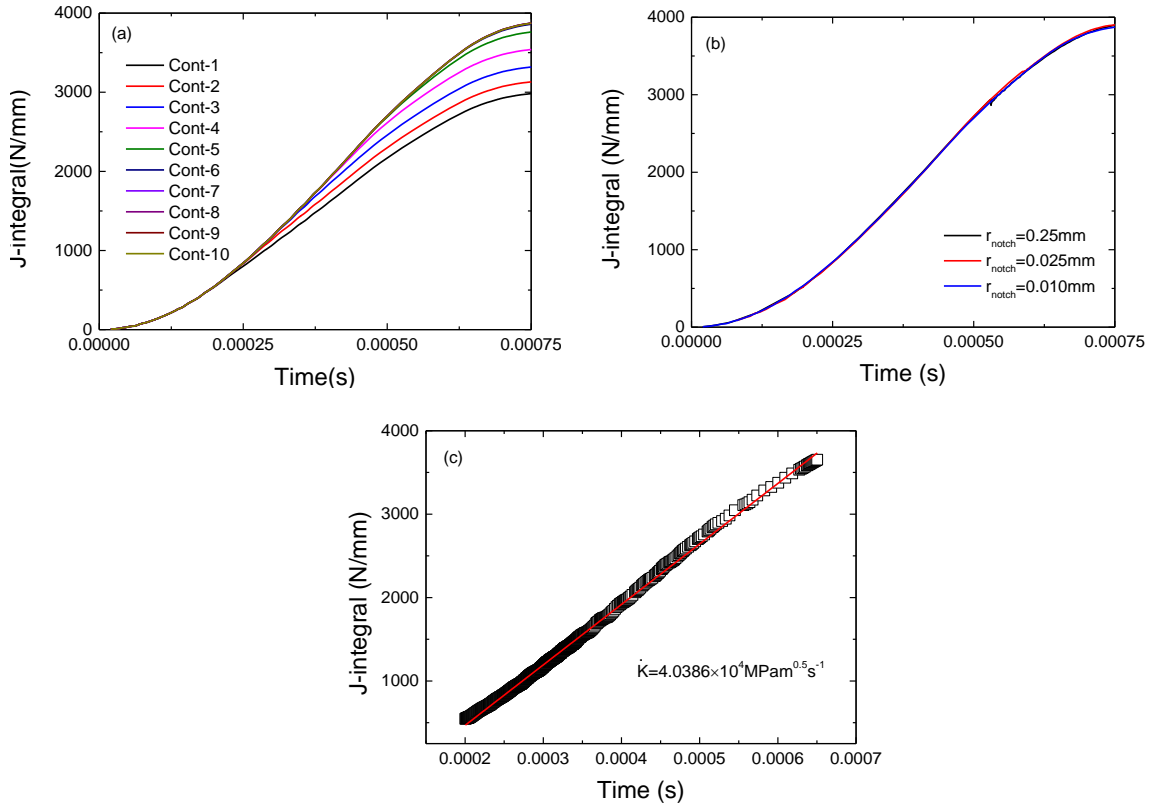
402 *Fig.8 the DBT curve of steel predicted by the continuum model with different elastic zone size. The*
 403 *loading rate is $10 MPam^{0.5}s^{-1}$.*

404

405 5.2.2 The temperature dependent effective surface energy

406 As mentioned above, the shielding effect of dislocation mobility on crack tip is loading rate dependent.
 407 To obtain the loading rate of Charpy impact test, the three-dimensional analysis of Charpy test is
 408 conducted. The geometry of Charpy V-notch specimen is identical to that introduced in the section 4.
 409 To model the transient process of impact and obtain the J-integral from Abaqus, a dynamic implicit
 410 process is utilized. However, only a stationary crack is studied here. The V-notch Charpy impact
 411 specimen is actually replaced by U-notch specimen in the calculation of J-integral since that the
 412 identical J-integrals calculated by Abaqus have been obtained from both notch-type specimen with
 413 same radius in present study. A path-independence pattern is presented in the Fig.9 (a) in a relative far
 414 field (beyond the 5 contours) near notch root. A notch radius independence of J-integrals is presented

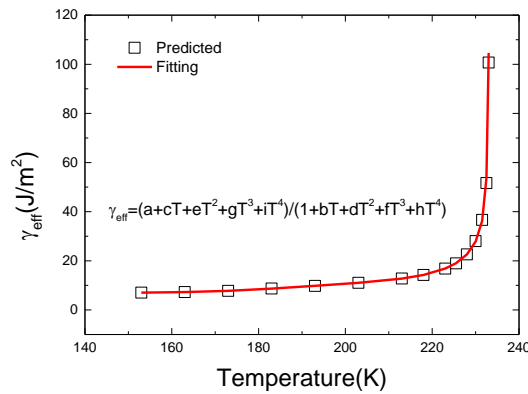
415 in Fig.9 (b). The loading rate \dot{K} of Charpy impact test, $4.0386 \times 10^4 \text{MPam}^{0.5} \text{s}^{-1}$, is achieved by fitting
 416 the linear part of the curve of J-integral vs. time as shown in Fig.9 (c).



417

418

419 *Fig.9 Charpy impact test modelling results: (a) path-independence of J-integral of U-notch specimen*
 420 *with notch radius 0.25mm, (b) J-integral of Charpy impact tests with different notch radius, (c) the*
 421 *loading rate of Charpy impact test. Here, r_{notch} is the notch radius of Charpy specimen.*



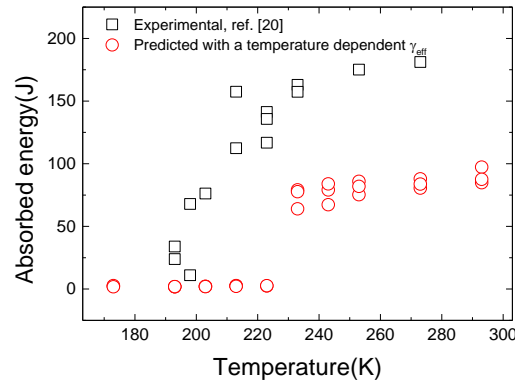
422

423 *Fig.10 the calculated effective surface energy in the transition region by using continuum model,*
 424 *where a, b, c, d, e, f, g, h, i are constant.*

425

426 By applying continuum approach shown in Section 3, the fracture toughness of the TMCR steel in the
 427 DBT region is calculated with parameters identified in section 5.2.1 and the loading rate of Charpy
 428 impact test calculated above. According to equation (8), the effective surface energy of TMCR steel in

429 the transition region is calculated as shown in Fig.10. It can be found that the effective surface energy
 430 of steel in the lower temperature, e.g. below 200K, is very stable and comparatively low. However, it
 431 increase rapidly until the critical DBT temperature when temperature beyond 220K. In addition, an
 432 equation for describing the correlation between the effective surface energy and temperature is
 433 obtained by fitting the calculated effective surface energy at different temperature, see Fig.10. This
 434 equation for temperature dependent effective surface energy will be adopted in the later simulation of
 435 DBT of TMCR steel.



436
 437 *Fig.11 absorbed energy of Charpy impact test in the transition region predicted by CAFE model with*
 438 *a temperature-dependent effective surface energy.*

439
 440 **5.3 DBT of TMCR steel modeled with an effective surface energy**

441 A temperature-dependent effective surface energy law obtained in Section 5.2 (see Fig.10) is applied
 442 to the CAFE method to simulate the DBT of TMCR steel. Here, the procedure and parameters used
 443 for the modelling are identical to those utilized in the Section 5.1 except that a constant value of the
 444 effective surface energy is replaced by the temperature-dependent effective surface energy. The
 445 predicted absorbed Charpy energy vs. temperature is plotted in the Fig.11, in which the experimental
 446 results are also presented for comparison. It can be observed that the DBT transition happens in a very
 447 narrow temperature range and a dramatic steep transition are obtained comparing with the
 448 experimental results. In addition, both lower shelf and upper shelf of DBT are obviously
 449 underestimated.

450 In the process of the unstable cleavage propagation of steel, the second step is critical in terms of the
 451 formation of unstable fracture [45], otherwise the crack stops or be blunted at the interface, and then
 452 the cracked particle may act as the nuclei for void growth when ductile fracture intervenes. The
 453 critical fracture stress for the crack propagation across the interface between the particle and matrix,
 454 e.g., particle cleavage strength σ_{pm} [46], can be calculated by

$$\sigma_{pm} = \left(\frac{\pi E \gamma_{pm}}{(1 - \nu^2)c} \right)^{1/2} \quad (12)$$

455 where γ_{pm} is the effective surface energy to propagate the micro-crack across particle-matrix interface;
 456 c is the particle size. Once unstable fracture formatted, e.g., micro-crack initiation from the particle
 457 and penetration into the matrix, the first grain boundary could be the barrier for unstable cleavage
 458 crack to trespass, see Fig.3 (a).The critical fractures stress, e.g. grain strength σ_{mm} [46], becomes a
 459 criterion for the extension of the crack across the grain boundary, which can be described as

$$\sigma_{mm} = \left(\frac{\pi E \gamma_{mm}}{(1 - \nu^2) d} \right)^{1/2} \quad (13)$$

460 where γ_{mm} is the effective surface energy for crack propagation across the grain boundary; d is grain
 461 size. Comparing with the equation (14), it indicates that

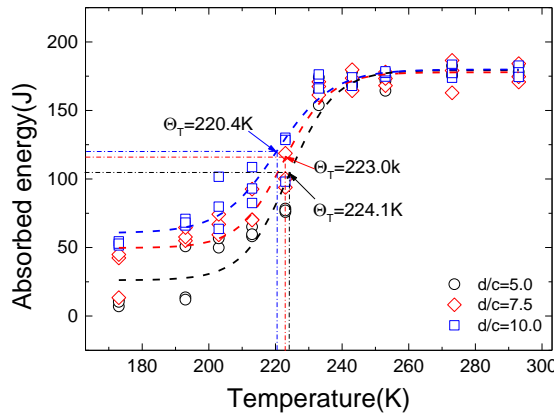
$$\frac{\sigma_{mm}}{\sigma_{pm}} = \frac{\gamma_{mm} c}{\gamma_{pm} d} \quad (14)$$

462 When the local stress near the particle $\sigma_L = \sigma_{mm} < \sigma_{pm}$, the micro-crack could propagate across the
 463 grain boundary, and unstable cleavage fracture would be ensured by the particle cracking. It implies
 464 that the unstable fracture is dominated by the particle size, e.g., cleavage at the lower shelf, where the
 465 local stress near the particle is high enough due to the higher yield stress. However, when $\sigma_L =$
 466 $\sigma_{mm} > \sigma_{pm}$, the crack arrests at the grain boundary, resulting in the appearance of stable and grain-
 467 sized micro-crack. It means that the propagation of unstable fracture is dominated by the grain size,
 468 e.g., cleavage occurring in the transition region, where the local stress near the particle is not adequate
 469 to overcome the grain strength. Therefore, it can be concluded that the role of grain boundary on the
 470 unstable cleavage propagation should not be neglected, and that the cleavage propagation in the
 471 transition region depends on the competition between σ_{mm} and σ_{pm} , e.g., particle dominated or grain
 472 size dominated [46-50].

473 A critical condition for crack propagating across the first grain boundary can be deduced from the
 474 equation (14) when σ_{mm} equals to σ_{pm} , from which the lower limit of the effective surface energy for
 475 crack extension across the grain boundary can be achieved

$$\gamma_{mm} = \gamma_{pm} \frac{d}{c} \quad (15)$$

476 It implies that the minimum of γ_{mm} is solely related the size ratio of grain and particle when the
 477 effective surface energy of cleavage formation of the material, e.g., γ_{pm} , has been obtained. As such,
 478 the γ_{pm} can be transferred to γ_{mm} , by using equation (15). Recall the equation (3), the γ_{mm} is exactly
 479 required to calculate the fracture stress of cleavage in CAFE model. While, the effective surface
 480 energy obtained in the section 5.2, it is actually not the γ_{mm} but the γ_{pm} , which is the reason why the
 481 absorbed energies in the full temperature range is underestimated as shown in the Fig.11.



482

483 *Fig.12 the predicted DBT of TMCR steel with different ratios of d/c . Here, data is fitted by the*
 484 *sigmoidal method. The transition temperature Θ_T is defined as the temperature corresponding to the*
 485 *impact energy halfway between the lower shelf energy (LSE) and USE [49].*

486

487 Based on the γ_{pm} obtained in Section 5.2, DBT of the TMCR steel is predicted with the variable ratio
 488 of d/c as shown in the Fig.12. It can be observed that different ratio of d/c can achieve a similar
 489 upper shelf, while the lower shelf and the absorbed energy in transition region are quite different.
 490 Since complete ductile fracture happens on the upper shelf, the ratio of d/c presents no effect on the
 491 absorbed energy, which is usually only relevant to the cleavage fracture. It is also found that the larger
 492 ratio of d/c enables a higher absorbed energy of steel in the temperature range below the upper shelf.
 493 Meanwhile, a lower transition temperature, Θ_T , is achieved for the larger ratio of d/c . San Martin et
 494 al. [47] has studied the cleavage fracture in the transition region of Ti-V alloyed steel, in which some
 495 isolated cleavage islands could be formed surrounded by ductile fracture. They have measured the
 496 sizes of cleavage islands, e.g., d_{CL} and the sizes of cleavage initiators, e.g. c_{crit} . The effective surface
 497 energy γ_{mm} has been calculated by using a similar transferring rule (e.g., equation (15)), in which the
 498 effective surface energy $\gamma_{pm} = 7 \text{ J/m}^2$ has been adopted. It has been found that the γ_{mm} lineally
 499 increases with the ratio of d_{CL}/c_{crit} . measured at all temperatures in DBT regime. This proves that the
 500 ratio d/c in equation (15) can physically reflect the toughness of material as shown in Fig.12.

501 It is well known that the particle precipitated in the steel is non-uniformly distributed for both size and
 502 spacing. Ahead of the crack/notch tip, the particle is sampled as the cleavage nucleate once the
 503 maximum principle stress ahead of the crack/notch tip is higher than σ_{pm} , see equation (12). However,
 504 the stress ahead of the crack/notch tip generally decreases with the temperature, which means that
 505 accordingly the size of qualified particle to be sampled as the initiator of cleavage decreases with the
 506 decrease of temperature. A linear relation between temperature and critical particle size has been
 507 found in SA 508 steel by Lee et al [51]. Since the grain size is temperature independent, it implies
 508 that the ratio of d/c is not a constant value in the transition regime but a variable relevant to the

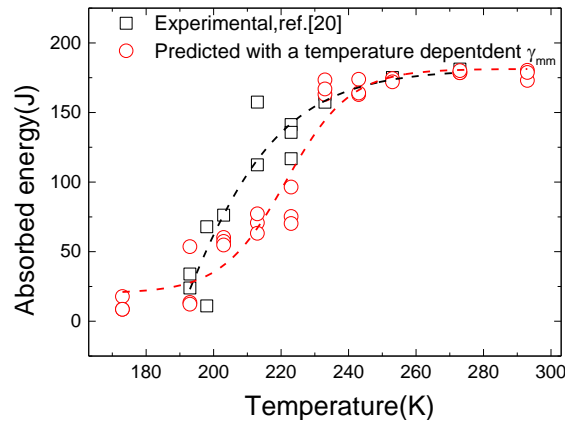
509 temperature. In addition, the crystallographic unit of cleavage could not be the grain size, since crack
 510 deflection or arrest usually does not happens at the lower grain boundary. Whilst, it has been pointed
 511 out that the cleavage fracture unit (facet) size or the effective grain size is more suitable to describe
 512 the cleavage fracture unit, and that both of them match each other very well in Mn-Mo-Ni low alloy
 513 steel [52]. To accurately describe the competition between σ_{pm} and σ_{mm} of cleavage fracture in the
 514 transition region, the grain size d in equation (15) should be modified to the cleavage facet (unit) size
 515 $d_{CF(U)S}$ or effective grain size d_{EGS} . According to the findings by Lee et al [51], a linear relation
 516 between the ratio of $d_{CF(U)S}/c_{crit.}$ or $d_{EGS}/c_{crit.}$ and temperature could be expected since that the
 517 $d_{CF(U)S}$ is generally temperature independent. To this end, a linear correlation between $d_{CF(U)S}/c_{crit.}$
 518 and temperature is assumed

$$\frac{d_{CF(U)S}}{c_{crit.}} = -0.025(\Theta - 273) + 4.0 \quad (16)$$

519 where Θ is temperature. Then, the effective surface energy obtained in section 5.2 as shown in Fig.10
 520 is corrected by the ratio of $d_{CF(U)S}/c_{crit.}$ in equation (16) according to the equation (15), from which
 521 the γ_{mm} can be obtained. Then, the calculated γ_{mm} is implemented in CAFE model to predict the
 522 DBT of TMCR steel. The predicted absorbed energy vs. temperature is plotted in the Fig.13, in which
 523 the experimental results of TMCR steel is also presented for comparison. It is observed that
 524 simulation is able to produce a full transition curve with a scatter pattern of absorbed energies in the
 525 transition region. Generally, the predicted transition curve is comparative to the experimental results.
 526 The simulation can reproduce a similar LSE and USE comparing with the experimental results, while
 527 the absorbed energy in transition region is slightly underestimated comparing with the experimental
 528 results.

529 It is not surprising for the underestimation of the absorbed energy in the transition region as shown in
 530 Fig.13 because that the γ_{mm} estimated from equation (15) is just its lower limit. Actually, it is very
 531 difficult to precisely measure or predict the effective surface energy for crack propagating across the
 532 grain boundary [47, 50]. In the section 5.2, a constant exponent m that describes the correlation
 533 between dislocation velocity and resolved shear stress is used to estimate the effective surface energy
 534 of unstable cleavage formation (e.g., the second step) in the transition region, see equation (6) and (7).
 535 However, it has been found that m decreases with the increase of temperature [53, 54], which means
 536 that the fracture toughness in transition region could be underestimated since the lower m can lead to a
 537 higher toughness [35] in the transition region. Accordingly, the γ_{pm} for cleavage penetration into
 538 matrix could be under-predicted as well. This could be a reason why the predicted absorbed energies
 539 in the transition region are lower than those of experimental results as shown in Fig.13. Since the
 540 lacking of the experimental correlation between the ratio of $d_{CF(U)S}/c_{crit.}$ and temperature for this
 541 TMCR steel, an artificial linear relation between them is assumed to transfer the γ_{pm} to γ_{mm} , which is

542 inspired by the study in ref. [51]. Therefore, measurements on the critical particle size and the
 543 cleavage facet (unit) size of steel have to be conducted so as to find a more reliable temperature
 544 dependent ratio of $d_{CF(U)S}/c_{crit}$.



545

546 *Fig.13 absorbed energy of Charpy impact test in the transition region predicted by CAFE model with*
 547 *a temperature-dependent effective surface energy corrected by a temperature dependent ratio of*
 548 *$d_{CF(U)S}/c_{crit}$. Here, data is fitted by the sigmoidal method.*

549

550

551 6. Conclusions

552 In this study the CAFE method developed by Shterenlikht et al [20-22] has been applied to mitigate
 553 some of the computational challenges in modelling of DBT and incorporate the statistical nature of
 554 microstructure at the same time. In order to realistically capture the temperature dependent fracture
 555 toughness in the transition region, a physical based variable has to be searched, which is also one of
 556 the motivations of this work. On the basis of our previous work [33] a continuum approach has been
 557 developed to estimate the effective surface energy for unstable cleavage formation, e.g., γ_{pm} . Further,
 558 to describe the essence of the competition between particle size and grain size-controlled propagation
 559 of unstable cleavage, a more robust variable, effective surface energy for overcoming the barrier of
 560 grain boundary, e.g., γ_{mm} , was proposed. Finally, a framework for the modelling of DBT is explored
 561 through implementing the γ_{mm} into the CAFE method. Some important findings obtained in present
 562 work can be summarized as followings:

- 563 • It is proved that a second temperature dependent variable has to be found to reproduce the
 564 DBT curve, in addition to the temperature dependent flow properties. In present work, a
 565 continuum approach has been developed to establish the second temperature dependent
 566 variable, e.g., γ_{pm} .

- 567 • It is observed that the role of grain boundary on the unstable cleavage propagation cannot be
568 ignored. Through analyzing the competition between the particle size and grain size
569 dominated unstable cleavage propagation, a method to quantify the lower limit of γ_{mm} has
570 been built.
- 571 • Due to the fact that cleavage facet (unit) size or effective grain size, e.g., $d_{CF(U)S}$, rather than
572 the grain size is more appropriate for characterizing the cleavage fracture unit, the ratio of
573 grain size to critical particle size has been replaced by $d_{CF(U)S}/c_{crit.}$ in the estimation of γ_{mm} .
- 574 • It is found that numerical simulation by using the CAFE method implemented with γ_{mm} is
575 able to produce a full transition curve, especially with scattered absorbed energies in the
576 transition region represented.

577 Although a framework of modelling DBT of steel is explored in this work, it still has some limitations.
578 More experimental results are required for the calibration of parameters to calculate the temperature
579 effective surface energy adopted in present work, for instance, the activation energy for the DBT and
580 the temperature dependent ratio of $d_{CF(U)S}/c_{crit.}$ of the TMCR steel. In addition, the adiabatic heating
581 effect and viscoplastic of material is not considered in Charpy impact modelling.

582

583

584 *Acknowledgements*

585 The authors wish to thank the Research Council of Norway for funding through the Petromaks 2
586 Programme, Contract No.228513/E30. The financial support from Eni, Statoil, Lundin, Total, JFE
587 Steel Corporation, Posco, Kobe Steel, SSAB, Bredero Shaw, Borealis, Trelleborg, Nexans, Aker
588 Solutions, FMC Kongsberg Subsea, Kværner Verdal, Marine Aluminium, Hydro and Sapa are also
589 acknowledged.

590

591

592 **References**

- 593 [1] A.L. Gurson, Continuum Theory of Ductile Rupture by Void Nucleation and Growth: Part I—
594 Yield Criteria and Flow Rules for Porous Ductile Media, *Journal of Engineering Materials and*
595 *Technology* 99(1) (1977) 2-15.
- 596 [2] V. Tvergaard, A. Needleman, Analysis of the cup-cone fracture in a round tensile bar, *Acta*
597 *Metallurgica* 32(1) (1984) 157-169.
- 598 [3] Z.L. Zhang, C. Thaulow, J. Ødegård, A complete Gurson model approach for ductile fracture,
599 *Engineering Fracture Mechanics* 67(2) (2000) 155-168.
- 600 [4] T. Pardoen, J.W. Hutchinson, An extended model for void growth and coalescence, *Journal of the*
601 *Mechanics and Physics of Solids* 48(12) (2000) 2467-2512.
- 602 [5] G. Rousselier, Ductile fracture models and their potential in local approach of fracture, *Nuclear*
603 *Engineering and Design* 105(1) (1987) 97-111.

604 [6] A. Pineau, A.A. Benzerga, T. Pardoen, Failure of metals I: Brittle and ductile fracture, *Acta*
605 *Materialia* 107 (2016) 424-483.

606 [7] R.O. Ritchie, J.F. Knott, J.R. Rice, On the relationship between critical tensile stress and fracture
607 toughness in mild steel, *Journal of the Mechanics and Physics of Solids* 21(6) (1973) 395-410.

608 [8] F.M. Beremin, A. Pineau, F. Mudry, J.-C. Devaux, Y. D'Escatha, P. Ledermann, A local criterion
609 for cleavage fracture of a nuclear pressure vessel steel, *Metallurgical Transactions A* 14(11) (1983)
610 2277-2287.

611 [9] T. Lin, A.G. Evans, R.O. Ritchie, A statistical model of brittle fracture by transgranular cleavage,
612 *Journal of the Mechanics and Physics of Solids* 34(5) (1986) 477-497.

613 [10] K. Wallin, T. Saario, K. Törrönen, Statistical model for carbide induced brittle fracture in steel,
614 *Metal Science* 18(1) (1984) 13-16.

615 [11] M.K. Samal, M. Seidenfuss, E. Roos, B.K. Dutta, H.S. Kushwaha, Experimental and numerical
616 investigation of ductile-to-brittle transition in a pressure vessel steel, *Materials Science and*
617 *Engineering: A* 496(1) (2008) 25-35.

618 [12] M.K. Samal, J.K. Chakravarty, M. Seidenfuss, E. Roos, Evaluation of fracture toughness and its
619 scatter in the DBTT region of different types of pressure vessel steels, *Engineering Failure Analysis*
620 18(1) (2011) 172-185.

621 [13] V. Tvergaard, A. Needleman, An analysis of the temperature and rate dependence of Charpy V-
622 notch energies for a high nitrogen steel, *International Journal of Fracture* 37(3) (1988) 197-215.

623 [14] V. Tvergaard, A. Needleman, An analysis of the brittle-ductile transition in dynamic crack
624 growth, *International Journal of Fracture* 59(1) (1993) 53-67.

625 [15] A. Needleman, V. Tvergaard, Numerical modeling of the ductile-brittle transition, *International*
626 *Journal of Fracture* 101(1) (2000) 73.

627 [16] A. Rossoll, C. Berdin, C. Prioul, Determination of the Fracture Toughness of a Low Alloy Steel
628 by the Instrumented Charpy Impact Test, *International Journal of Fracture* 115(3) (2002) 205-226.

629 [17] B. Tanguy, J. Besson, R. Piques, A. Pineau, Ductile to brittle transition of an A508 steel
630 characterized by Charpy impact test: Part I: experimental results, *Engineering Fracture Mechanics*
631 72(1) (2005) 49-72.

632 [18] B. Tanguy, J. Besson, R. Piques, A. Pineau, Ductile to brittle transition of an A508 steel
633 characterized by Charpy impact test: Part II: modeling of the Charpy transition curve, *Engineering*
634 *Fracture Mechanics* 72(3) (2005) 413-434.

635 [19] G. Hütter, T. Linse, S. Roth, U. Mühlich, M. Kuna, A modeling approach for the complete
636 ductile–brittle transition region: cohesive zone in combination with a non-local Gurson-model,
637 *International Journal of Fracture* 185(1) (2014) 129-153.

638 [20] A. Shterenlikht, I.C. Howard, The CAFE model of fracture—application to a TMCR steel,
639 *Fatigue & Fracture of Engineering Materials & Structures* 29(9-10) (2006) 770-787.

640 [21] A. Shterenlikht, 3D CAFE modelling of transitional ductile-brittle fracture in steel, The
641 University of Sheffield, UK, 2003.

642 [22] A. Shterenlikht, I.C. Howard, Cellular Automata Finite Element (CAFE) modelling of
643 transitional ductile-brittle fracture in steel, The 15th European Conference of Fracture (ECF15), KTH,
644 Stockholm, Sweden, 2004.

645 [23] S.J. Wu, C.L. Davis, A. Shterenlikht, I.C. Howard, Modeling the ductile-brittle transition
646 behavior in thermomechanically controlled rolled steels, *Metall and Mat Trans A* 36(4) (2005) 989-
647 997.

648 [24] S. Das, A. Shterenlikht, I.C. Howard, E.J. Palmiere, A general method for coupling
649 microstructural response with structural performance, *Proceedings of the Royal Society A:*
650 *Mathematical, Physical and Engineering Science* 462(2071) (2006) 2085-2096.

651 [25] A. Shterenlikht, L. Margetts, Three-dimensional cellular automata modelling of cleavage
652 propagation across crystal boundaries in polycrystalline microstructures, *Proceedings of the Royal*
653 *Society of London A: Mathematical, Physical and Engineering Sciences* 471(2177) (2015).

654 [26] Standard Test Method for Determination of Reference Temperature, T₀, for Ferritic Steels in the
655 Transition Range (ASTM E1921-18), American Society for Testing and Materials, 2018.

656 [27] J.P. Petti, R.H. Dodds, Calibration of the Weibull stress scale parameter, σ_u , using the Master
657 Curve, *Engineering Fracture Mechanics* 72(1) (2005) 91-120.

658 [28] B. Wasiluk, J.P. Petti, R.H. Dodds, Temperature dependence of Weibull stress parameters:
659 Studies using the Euro-material, *Engineering Fracture Mechanics* 73(8) (2006) 1046-1069.

660 [29] Y. Cao, H. Hui, G. Wang, F.-Z. Xuan, Inferring the temperature dependence of Beremin
661 cleavage model parameters from the Master Curve, *Nuclear Engineering and Design* 241(1) (2011)
662 39-45.

663 [30] G. Qian, V.F. González-Albuixech, M. Niffenegger, Calibration of Beremin model with the
664 Master Curve, *Engineering Fracture Mechanics* 136 (2015) 15-25.

665 [31] X. Gao, G. Zhang, T.S. Srivatsan, A probabilistic model for prediction of cleavage fracture in the
666 ductile-to-brittle transition region and the effect of temperature on model parameters, *Materials*
667 *Science and Engineering: A* 415(1) (2006) 264-272.

668 [32] M. Moattari, I. Sattari-Far, I. Persechino, N. Bonora, Prediction of fracture toughness in ductile-
669 to-brittle transition region using combined CDM and Beremin models, *Materials Science and*
670 *Engineering: A* 657 (2016) 161-172.

671 [33] Y. Li, X. Ren, J. He, Z. Zhang, Constraint effect on the brittle-to-ductile transition of single-
672 crystal iron induced by dislocation mobility, *International Journal of Mechanical Sciences* 149 (2018)
673 212-223.

674 [34] M. Stec, J. Faleskog, Micromechanical modeling of grain boundary resistance to cleavage crack
675 propagation in ferritic steels, *International Journal of Fracture* 160(2) (2009) 151.

676 [35] V.R. Nitzsche, K.J. Hsia, Modelling of dislocation mobility controlled brittle-to-ductile transition,
677 *Materials Science and Engineering: A* 176(1) (1994) 155-164.

678 [36] A. Hartmaier, P. Gumbsch, Thermal activation of crack-tip plasticity: The brittle or ductile
679 response of a stationary crack loaded to failure, *Physical Review B* 71(2) (2005) 024108.

680 [37] A.S. Argon, Mechanics and Physics of Brittle to Ductile Transitions in Fracture, *Journal of*
681 *Engineering Materials and Technology* 123(1) (2000) 1-11.

682 [38] ASTM E23-18 Standard Test Methods for Notched Bar Impact Testing of Metallic Materials,
683 2018.

684 [39] A. Giannattasio, M. Tanaka, T.D. Joseph, S.G. Roberts, An empirical correlation between
685 temperature and activation energy for brittle-to-ductile transitions in single-phase materials, *Physica*
686 *Scripta* 2007(T128) (2007) 87.

687 [40] M. Tanaka, K. Higashida, T. Shimokawa, T. Morikawa, Brittle-Ductile Transition in Low
688 Carbon Steel Deformed by the Accumulative Roll Bonding Process, *MATERIALS*
689 *TRANSACTIONS* 50(1) (2009) 56-63.

690 [41] P.B. Hirsch, S.G. Roberts, The brittle-ductile transition in silicon, *Philosophical Magazine A*
691 64(1) (1991) 55-80.

692 [42] G.W. Hollenberg, G.R. Terwilliger, R.S. Gordon, Calculation of Stresses and Strains in Four-
693 Point Bending Creep Tests, *Journal of the American Ceramic Society* 54(4) (1971) 196-199.

694 [43] T. Fett, Stress Intensity Factors – T-Stresses – Weight Functions, Supplement Volume, KIT
695 Scientific Publishing, 2009.

696 [44] P. Bowen, S.G. Druce, J.F. Knott, Effects of microstructure on cleavage fracture in pressure
697 vessel steel, *Acta Metallurgica* 34(6) (1986) 1121-1131.

698 [45] M. Kroon, J. Faleskog, Micromechanics of cleavage fracture initiation in ferritic steels by carbide
699 cracking, *Journal of the Mechanics and Physics of Solids* 53(1) (2005) 171-196.

700 [46] T. Lin, A.G. Evans, R.O. Ritchie, Stochastic modeling of the independent roles of particle size
701 and grain size in transgranular cleavage fracture, *Metall and Mat Trans A* 18(4) (1987) 641-651.

702 [47] J.I. San Martin, J.M. Rodriguez-Ibabe, Determination of energetic parameters controlling
703 cleavage fracture in a Ti-V microalloyed ferrite-pearlite steel, *Scripta Materialia* 40(4) (1999) 459-464.

704 [48] L. Rancel, M. Gómez, S.F. Medina, I. Gutierrez, Measurement of bainite packet size and its
705 influence on cleavage fracture in a medium carbon bainitic steel, *Materials Science and Engineering:*
706 *A* 530 (2011) 21-27.

707 [49] A. Ghosh, A. Ray, D. Chakrabarti, C.L. Davis, Cleavage initiation in steel: Competition between
708 large grains and large particles, *Materials Science and Engineering: A* 561 (2013) 126-135.

709 [50] M.A. Linaza, J.M. Rodriguez-Ibabe, J.J. Urcola, DETERMINATION OF THE ENERGETIC
710 PARAMETERS CONTROLLING CLEAVAGE FRACTURE INITIATION IN STEELS, *Fatigue &*
711 *Fracture of Engineering Materials & Structures* 20(5) (1997) 619-632.

- 712 [51] S. Lee, S. Kim, B. Hwang, B.S. Lee, C.G. Lee, Effect of carbide distribution on the fracture
713 toughness in the transition temperature region of an SA 508 steel, *Acta Materialia* 50(19) (2002)
714 4755-4762.
- 715 [52] S. Kim, S. Lee, B.S. Lee, Effects of grain size on fracture toughness in transition temperature
716 region of Mn–Mo–Ni low-alloy steels, *Materials Science and Engineering: A* 359(1) (2003) 198-209.
- 717 [53] H.W. Schadler, Mobility of edge dislocations on {110} planes in tungsten single crystals, *Acta*
718 *Metallurgica* 12(8) (1964) 861-870.
- 719 [54] H.A. Khater, D.J. Bacon, Dislocation core structure and dynamics in two atomic models of α -
720 zirconium, *Acta Materialia* 58(8) (2010) 2978-2987.

721

CAFE based Multi-scale Modelling of Ductile-to-Brittle Transition of Steel with a Temperature Dependent Effective Surface Energy

Yang Li¹, Anton Shterenlikht², Xiaobo Ren³, Jianying He¹, Zhiliang Zhang^{1,*}

¹ NTNU Nanomechanical Lab, Department of Structural Engineering, Norwegian University of Science and Technology (NTNU), Richard Brikelands vei 1A, N-7491 Trondheim, Norway

² Department of Mechanical Engineering, University of Bristol, University Walk, Bristol

³ SINTEF Industry, Richard Brikelands vei 2B, N-7465 Trondheim, Norway

Abstract: *It is still a challenge to numerically achieve the interactive competition between ductile damage and brittle fracture in ductile-to-brittle transition (DBT) region. In addition, since two types of fracture occur at two independent material length scales, it is difficult to process them with the same mesh size by using finite element method. In this study, a framework of modelling DBT of a thermal mechanical controlled-rolling (TMCR) steel is explored by using the cellular automata finite element (CAFE) method. The statistical feature of material's microstructure is incorporated in the modelling. It is found that DBT curve cannot be reproduced with only one temperature dependent flow property, for which another temperature dependent variable must be considered. A temperature dependent effective surface energy based on typical cleavage fracture stage is proposed and obtained through a continuum approach in present work. The DBT of TMCR steel is simulated by using CAFE method implemented with a temperature dependent effective surface energy. It is found that numerical simulation is able to produce a full transition curve, especially with scattered absorbed energies in the transition region represented. It is also observed that simulation results can reproduce a comparable DBT curve contrasting to the experimental results.*

Keywords: Cellular Automata Finite Element (CAFE); Ductile-to-Brittle Transition (DBT); Cleavage; Effective surface energy; TMCR steel

1. Introduction

Ductile-to-brittle transition (DBT) is normally found in the BCC materials, e.g., steel, due to temperature decreasing and loading rate elevation. Ductile fracture usually occurs at higher temperature, e.g. the upper-shelf, with a damage mechanism of void nucleation, growth and coalescence. The well-known Gurson type of model [1-4] and Rousselier model [5] have been widely used to describe ductile fracture accompanying with plastic deformation, in which the critical void volume fraction f_c has been proposed as the failure criterion. While, unstable cleavage fracture is

35 commonly initiated by second-phase particle cracking due to dislocation pile-up, which refers to the
36 sequence of three steps: particle breakage, transgranular fracture within a single grain and overcoming
37 of the grain boundary [6]. A simple model proposed by Ritchie, Knott and Rice [7], so called RKR
38 model, assumes that cleavage failure occurs when the maximum principle stress ahead of the crack tip
39 exceeds the fracture stress σ_f over a characteristic distance. In order to describe the statistical nature
40 of micro-cracks in the stress field, micromechanical models [8-10] following the weakest link
41 philosophy have been reformulated based on RKR model, which provide a promising local approach
42 to understand the essentials of cleavage. One of the most widely used approaches is Beremin model
43 [8], in which a simple expression for macroscopic failure probability can be derived involving a scalar
44 measure of the crack-front loading, the so-called Weibull stress σ_w . Consequently, two main types of
45 the failure criterion for cleavage have been established, critical fracture stress σ_f or Weibull stress σ_w .
46 Whereas, in the DBT regime, two fracture modes coexist, and the final rupture of materials occurs as
47 a consequence of the competition between two failure mechanisms.

48 Modelling of DBT of steel has aroused great interest in past decades. Ductile damage models (e.g.,
49 GTN, Rousselier) combined with RKR criterion model or local approach (e.g. Beremen model) has
50 been widely applied to model the DBT of steel under quasi-static load [11, 12] or dynamic load [13-
51 18]. However, it is basically a post-processing solution to evaluate the occurrence of cleavage after
52 stress field ahead of crack tip obtained from the constitutive equation of ductile model. The
53 competition between two failure mechanisms and the interaction between two failure modes in the
54 transition region are not involved indeed. Furthermore, the fracture in the transition region occurs on
55 two independent scales of microstructure size, ductile fracture related to the spacing of the dominant
56 void initiated from particles, while the brittle fracture related to the grain or cleavage facet size. It is
57 difficult to handle two fracture modes with only one mesh size using the finite element method.
58 Although attempts have been conducted to overcome this problem by using non-local approaches [11,
59 12, 19], it is still a challenge to represent the competition between two failure mechanisms and the
60 interaction between two failure modes in the transition region. However, one approach coupled
61 cellular automata (CA) and finite element (FE), so-called CAFE method, provides a practical solution
62 to solve these two challenges simultaneously [20]. In addition, the statistical feature of microstructure
63 of material can also be represented in this method, e.g. initial void distribution, grain size distribution,
64 misorientation of grain boundaries etc., such that the scatter of toughness in the transition region can be
65 captured. The principle and implementation of CAFE method have been thoroughly described in the
66 ref. [20-25].

67 It is known that the flow properties, e.g., yield stress and strain hardening, will be altered as
68 temperature decreases, which could be a significant factor resulting in the occurrence of DBT.
69 However, only temperature-dependent flow stress is not enough to predict the transition behavior of
70 materials when comparing with the test data reported by Rossoll et al [16], Tanguy et al [18] and

71 Shterenlikht et al [20]. Many efforts have been made to describe temperature dependence of fracture
72 toughness in the DBT transition region. A global approach, Master curve method has been adopted in
73 ASTM E1921 [26], in which the variation of fracture toughness with temperature in DBT region can
74 be described with a reference temperature T_0 . Although the Master curve method is very convenient
75 to apply in practice since only few tests are needed for calibration, it requires high constraint and
76 small scale yielding conditions. Tanguy et al [18] has simulated the DBT of A508 steel with a
77 temperature-dependent σ_u rather than a constant value when modelling the Charpy impact test. By
78 using Master curve method [26] to calibrate the parameters of Beremin model, Petti et al [27],
79 Wasiluk et al [28], Cao et al [29] and Qian et al [30] have also found that σ_u is increasing with
80 temperature in the transition region. Gao et al [31] has found that σ_u increased with temperature
81 reflecting the combined effects of temperature on material flow properties and toughness. Moattari et
82 al[32] accurately predicted the fracture toughness in DBT transition region by introducing a
83 temperature-dependent σ_u described with a summation of athermal and thermally activated stress
84 contribution. A temperature dependent misorientation of grain boundary proposed by Shterenlikht et
85 al [20] has been implemented into the CAFE method to model the DBT of Charpy test of TMCR steel.
86 It has to be noticed that either the temperature dependent σ_u or misorientation proposed in the
87 literature is just a phenomenological parameter for DBT modelling. Therefore, exploring a physical-
88 based variable to disclose the nature of temperature dependent fracture toughness in the transition
89 region is not only significant but also necessary. In this work, on the basis of our previous work [33],
90 a continuum approach is developed to estimate the effective surface energy in the DBT transition
91 region of a TMCR steel. Then, we attempt to establish a framework of numerical prediction of the
92 DBT in steel by utilizing the CAFE method implemented with the temperature dependent effective
93 surface energy.

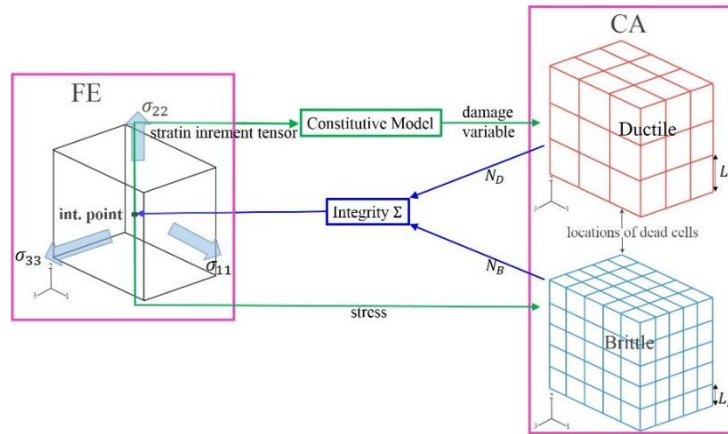
94 The present paper is organized as the followings. Section 2 reviews the CAFE method and discusses
95 the parameters of the model. Section 3 introduces a continuum solution to determine the temperature
96 dependent effective surface energy of TMCR steel. Section 4 describes the finite element procedures
97 and models used to predict the DBT of steels. Section 5 presents the main modelling results of DBT
98 of Charpy tests by using CAFE method implemented with a temperature dependent effective surface
99 energy. The physical nature of the competition between particle size dominated and grain size
100 dominated cleavage propagation is also discussed. The feasibility of CAFE method implemented with
101 temperature dependent effective surface energy is validated by comparing the predicted results to
102 experimental results in the literature [20]. Section 6 ends the paper with a short summary and
103 conclusions.

104

105

1106 **2. The CAFE Method**

1107 The motivation of the CAFE method is to combine the structural and microstructural interactions by
 1108 finite element method [20-22]. The method is divided into two phases: one is finite elements to
 1109 capture the stresses or strains at the structural level, the other is to catch the mechanical essentials of
 1110 the microstructural behavior and its development in a set of CA arrays. Fig.1 shows the
 1111 implementation of the above strategy to deal with the fracture in the transition region where both
 1112 ductile and brittle micro-mechanisms work simultaneously [20]. In each material integration point, the
 1113 microstructure is represented by two CA arrays, where the brittle array represents the cleavage
 1114 behavior while the ductile array processes ductile damage. Structural information, for example,
 1115 stress/strain and damage variable, processed in FE level inputs to CA levels, meanwhile, the
 1116 microstructural evolution and the failure are integrated and send back to the FEs. To achieve the
 1117 implementation of CAFE method in finite element, the explicit dynamic process has been chosen to
 1118 develop a VUMAT by Shterenlikht et al [20-22] so that crack can propagate along a natural failure
 1119 path through element removal.



120
 121 *Fig.1 the illustration of the mechanism of CAFE model in which ductile damage and cleavage*
 122 *fracture have been coupled through two different CA arrays. Here, where N_D and N_B are the number*
 123 *of 'dead' cell of ductile CA arrays and brittle CA arrays respectively; Σ is integration indicator; L_D*
 124 *and L_B are the size of cells in brittle and ductile CA arrays.*

125
 126 The Rousellier ductile damage model [5] is adopted to describe the constitutive response at the
 127 integration point. Equation (1) describes the plastic potential of this model

128
$$\frac{\sigma_{eq}}{\rho} - H(\varepsilon_{eq}) + B(\beta)Dexp\left(\frac{\sigma_m}{\rho\sigma_1}\right) = 0 \quad (1)$$

129 where $H(\varepsilon_{eq})$ is the hardening property of material; σ_1 and D are material constants that need to be
 130 tuned; σ_{eq} , σ_m and ε_{eq} are equivalent stress, mean stress and equivalent strain; $B(\beta)$ is the function of
 131 damage variable β ; ρ is relative density, which can be described by

$$\rho = \frac{1}{1 - f_0 + f_0 \exp \beta} \quad (2)$$

132 where f_0 is initial void volume fraction. In ductile CA arrays, cell size L_D is used to characterize the
 133 unit cell size of ductile damage of material with a single void, which normally relates to the spacing of
 134 inclusions or large carbides in steel.

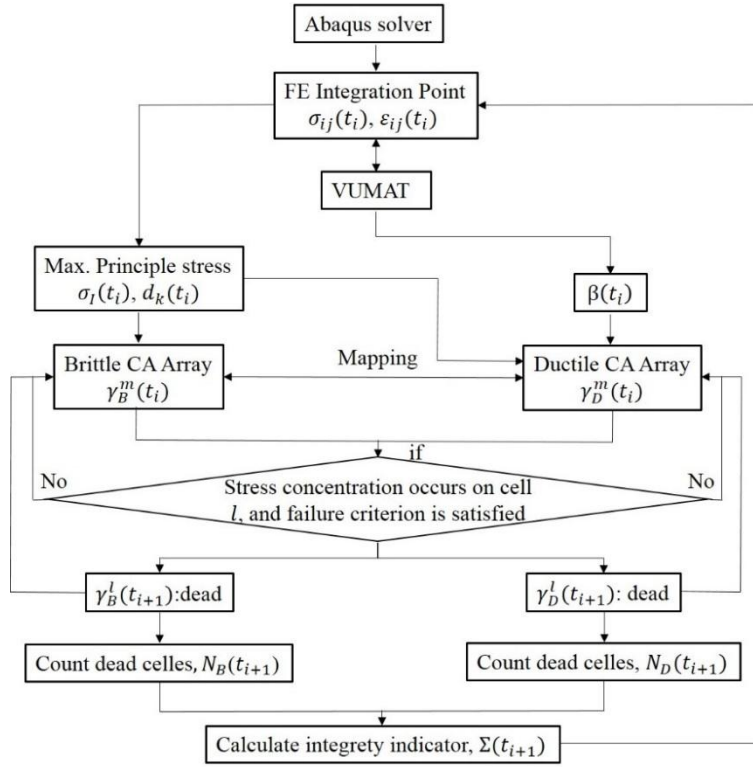
135 According to modified Griffith theory, the critical fracture stress for cleavage can be calculated by

$$\sigma_F = \sqrt{\frac{\pi E \gamma_{eff}}{(1 - \nu^2) d}} \quad (3)$$

136 where γ_{eff} is effective surface energy for the cleavage fracture; E and ν are Young's modulus and
 137 Poisson's ratio respectively; d is grain size. In present work, a temperature dependent effective
 138 surface energy for cleavage will be applied in the CAFE method to calculate critical fracture stress of
 139 cleavage. A fraction of brittle cells, η , in each brittle CA array, is adopted to represent grains with
 140 adjacent grain boundary carbides, where micro-crack has already nucleated. In brittle CA arrays, the
 141 cleavage facet size (d_{CFS}) is applied as the size of cells in brittle CA arrays, e.g. L_B , which can be
 142 measured through fractographic analysis on the fracture surface of specimen [20]. Since the
 143 misorientation between grains is naturally the barrier of cleavage crack propagation crossing the grain
 144 boundary [34], a random orientation is assigned to each cell in brittle CA arrays, and a misorientation
 145 threshold, e.g., θ_{th} , is assumed so that crack can propagate from one cell to the other.

146 The property of CA depends on the state of cells. The state of each cell in next time increment is
 147 determined by its state and the states of neighboring cells at the previous time increment. Once that
 148 the cell is failed due to the fracture propagation, the state of cell will be changed from 'alive', e.g.,
 149 initial state, to 'dead'. Then, the closing neighborhood of 'dead' cell will be stress-concentrated since
 150 the 'dead' cell lost its load-bearing capacity. A framework [22, 25] has described in detail how to
 151 locate such a closing neighborhood around the 'dead' cell. The local concentration factors are utilized
 152 to solve this problem, which are C_D for ductile CA array and C_B for brittle CA array. Thus, at the next
 153 time increment, the states of concentrated cells (either ductile or brittle) are determined by the results
 154 of comparison between the product of damage variable and concentration factors and failure criteria
 155 mentioned above. An integrity indicator, Σ , is used to count the 'dead' cells of both ductile and brittle
 156 CA arrays by which the potential fracture at every current time increment is evaluated. The Σ whose
 157 initial value is 1.0, decreases continuously with the accumulation of damage until N_D or N_B reaches
 158 its maximum value N_{D-max} or N_{B-max} . At this moment, the Σ turns to be zero, which means material
 159 inside the integration point is failed and the integration point does not have loading-bearing capacity
 160 any more. The FE will then be removed from the mesh when the zero Σ is transferred to FE. The Σ
 161 can be calculated by

$$\Sigma = 1 - \max\left(\frac{N_D}{N_{D-max}}, \frac{N_B}{N_{B-max}}\right) \quad (4)$$



162

163 *Fig.2 flow chart of the CAFE method. Here, $\sigma_{ij}(t_i)$ and $\epsilon_{ij}(t_i)$ are stress and strain tensors at time t_i*
 164 *provided by Abaqus solver; and $\beta(t_i)$ is damage variable of cells given by constitutive model to*
 165 *ductile CA array at time t_i ; $\sigma_I(t_i)$ is the maximum principle stress of each element calculated from*
 166 *$\sigma_{ij}(t_i)$; $d_k(t_i)$ is the direction cosines of $\sigma_I(t_i)$; $\gamma_D^m(t_i)$ or $\gamma_B^m(t_i)$ is state of cell m in ductile or*
 167 *brittle CA arrays t_i ; $\gamma_D^l(t_{i+1})$ or $\gamma_B^l(t_{i+1})$ is state of cell l where stress concentration occurs and*
 168 *failure criterion is satisfied in ductile or brittle cell arrays at time t_{i+1} ; $N_D(t_{i+1})$ or $N_B(t_{i+1})$ is*
 169 *numbers of dead cells in ductile or brittle CA arrays at time t_{i+1} ; $\Sigma(t_{i+1})$ is the integrity indicator at*
 170 *time at time t_{i+1} .*

171

172 The calculation process of the CAFE method is presented in Fig.2. It has to be mentioned that in order
 173 to reduce the calculation time, the damage variable $\beta(t_i)$ is given to the ductile CA array instead of
 174 the strain increment tensor $\Delta\epsilon_{ij}(t_i)$, and accordingly only the solution dependent variable Σ is
 175 returned to the FE from CA array. Both ductile and brittle CA arrays are used only for the simulation
 176 of fracture propagation at each CA scale, while, the constitutive response is calculated at FE level. In
 177 addition, for the easy achievement of convergence, in ductile CA array a normal distribution of
 178 damage value β_F rather than that of f_0 is adopted. At each increment of deformation, the model
 179 compares the present damage variable β with the failure value β_F until the material failed. Since two

180 CA arrays occupy the same physical space, the evaluation of the cells shall be synchronized in both
 181 CA arrays. Thus, a mapping rule has been introduced in the CAFE method to reflect dead cells in
 182 ductile CA array into the corresponding brittle CA array, and vice versa [21]. After stress
 183 concentration occurred on the cell m in either CA arrays, it becomes dead when failure criteria are
 184 satisfied. A more detailed description about the CAFE method can be found in literature [21].

185

186

187 3. The Temperature dependent effective surface energy

188 Based on the theory of shielding effect of dislocation mobility on crack tip, a method has been
 189 proposed [33] to predict the temperature dependent effective surface energy of single-crystal iron in
 190 the ductile-to-brittle transition (DBT) region. In the present work, this method will be extended to
 191 calculate the effective surface energy of steel in the transition region.

192 The shielding effect of the dynamics of dislocation on crack tip stress field can be assessed with a
 193 continuum method [33, 35, 36]. It is assumed that the material is isotropic, and that the rate-dependent
 194 plastic deformation is induced by dislocation emission and motion. According to Orowan law, the
 195 shear strain rate, $\dot{\gamma}^p$, can be used to describe the plasticity caused by the dislocation mobility

$$\dot{\gamma}^p = \alpha \rho_d b v \quad (5)$$

196 Where α is a proportionality constant; ρ_d is the dislocation density; b is Burgers vector; v is
 197 dislocation velocity. The dislocation velocity v can be obtained from the function of resolved shear
 198 stress τ and temperature Θ , e.g., the empirical Arrhenius type law

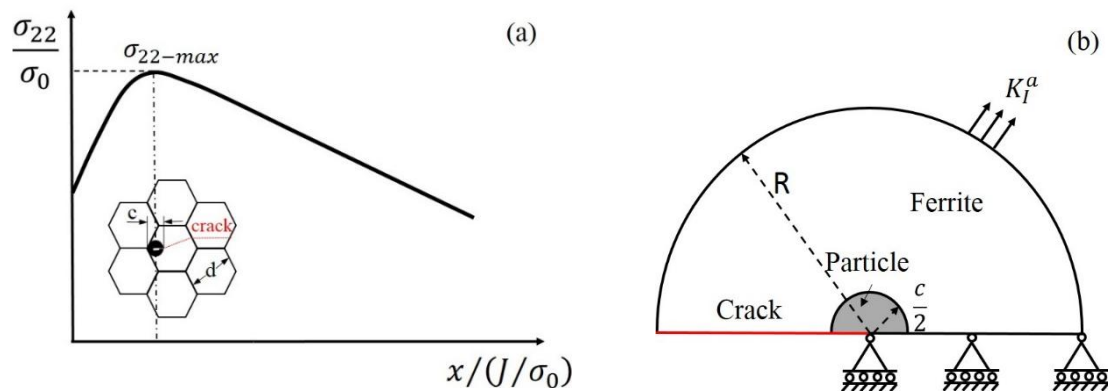
$$v = v_0 \exp\left(-\frac{Q}{k_B \Theta}\right) \left(\frac{\tau}{\tau_0}\right)^m \quad (6)$$

199 where Q is the activation energy for dislocation velocity; k_B is the Boltzmann constant; m is a
 200 material constant for wide range of stress level; v_0 is material specific reference dislocation velocity;
 201 τ_0 is normalization shear stress; here Θ is the absolute temperature in Kelvin. Since the material is
 202 assumed to be isotropic, the von Mises equivalent stress σ_{Mis} and the equivalent plastic strain
 203 rate $\dot{\epsilon}^p$ can be used to replace the plastic shear strain rate $\dot{\gamma}^p$ in equation (5) and the resolved shear
 204 stress τ in equation (6). Then, after inserting the equation (6) into equation (5), the equivalent plastic
 205 strain rate $\dot{\epsilon}$ to describe the rate-dependent plasticity induced by the dislocation mobility can be
 206 derived

$$\dot{\epsilon} = \dot{\epsilon}_0 \exp\left(-\frac{Q}{k_B \Theta}\right) \left(\frac{\sigma_{Mis}}{\sigma_0}\right)^m \quad (7)$$

207 where $\dot{\epsilon}_0$ is a reference strain rate; σ_0 is a normalization stress.

208 It is known that DBT normally occurs in body centered cubic (BCC) metals, e.g., single-crystal iron,
 209 Fe alloys and steel, due to the thermal-activated dislocation emission and motion [37]. The difference
 210 between single-crystal iron and steel is the presence of impurities (e.g., particles), grain boundary and
 211 preexisting dislocations in the latter, which affects the dislocation behavior, for instance, nucleation,
 212 motion, multiplication etc. If their effect on the fracture of the latter can be described by the change of
 213 dislocation density near crack tip comparing with that of former, see equation (5), the model
 214 developed for single-crystal iron is possible to be applied to the steel according to the theory of the of
 215 shielding effect of dislocation mobility on crack tip. To do this, several assumptions have to be made.
 216 Firstly, a micro-crack is assumed to be initiated within a grain boundary particle, e.g., carbide or
 217 inclusion, at a position x_c ahead of the notch/crack tip where the local tensile stress equals to the
 218 maximum principle stress, see Fig.3 (a). Then, the nucleated micro-crack will penetrate the interface
 219 between particle and matrix once that local tensile stress at interface exceeds the fracture stress.
 220 Secondly, we postulate that the penetration of the micro-crack into the interface leads to the final
 221 unstable cleavage fracture, namely the crack resistance of grain boundary is not taken into account.
 222 Further, it is assumed that the crack penetration from particle into matrix is dominated by a local K -
 223 field. Then, the elastic zone (dislocation free zone) in the continuum model for single-crystal material
 224 [33] is replaced with an elastic particle, and the viscoplastic material outside the elastic region is
 225 defined as the ferrite, e.g., a time-dependent plastic matrix. Thus, a new continuum model can be
 226 adopted to estimate the fracture toughness of steel in the transition region, see Fig.3 (b).



227

228 **Fig.3 the continuum model: (a) the schematic illustration of the micro-crack initiation and**
 229 **propagation across the interface and grain boundary, c is the particle diameter, and d is grain size;**
 230 **(b) MBL model to calculate the effective surface energy for cleavage extension across the interface**
 231 **between particle and matrix [33]. c is particle size.**

232

233 Only the upper-half of model is presented due to symmetry, see Fig.3 (b). A small circle around the
 234 crack tip with a radius $c/2$ is the elastic zone, e.g., particle. The radius of model R is 20 times larger
 235 than the elastic zone size. Outside the elastic zone, there is the matrix, e.g., ferrite, which is time-

236 dependent plastic material described by the equation (7). A crack with an initial radius of $1.15 \times$
 237 $10^{-4}R$ is located in the center of model. Abaqus 6.14 is employed, and 4-node and plane strain
 238 elements (CPE4) are used in all simulations. Through the nodal displacement on the outer boundary
 239 layer in the MBL model, a linear elastic K_I field, e.g., the applied stress intensity factor K_I^a , with a
 240 constant loading rate \dot{K} is implemented. To calculate the effective surface energy, only a stationary
 241 crack is studied.

242 For a sharp crack tip, cleavage fracture occurs once the crack tip stress intensity factor equals to the
 243 critical value, i.e. $K_I^t = K_{IC}$. The critical stress intensity factor K_{IC} depends only on the material's
 244 surface energy γ_s in terms of the Griffith criterion. Due to the shielding effect of plastic deformation
 245 on the crack tip stress field, the local stress intensity factor K_I^t at crack tip is always lower than the
 246 applied stress intensity factor K_I^a , particularly at higher temperature. The applied stress intensity
 247 factor K_I^a at the moment of failure, e.g. $K_I^t = K_{IC}$ is regarded as the fracture toughness of material.
 248 According to modified Griffith theory, $G_c = 2(\gamma_s + \gamma_p)$, if let $\gamma_s + \gamma_p = \gamma_{eff}$, the effective surface
 249 energy can be obtained by

$$\gamma_{eff} = \frac{(1 - \nu^2)}{2E} K^2 \quad (8)$$

250 Thus, the applied stress intensity factor K_I^a at cleavage fracture can be calculated, and
 251 accordingly the effective surface energy for cleavage extension across the particle-matrix
 252 interface of steel in the transition region can also be obtained from equation (8).

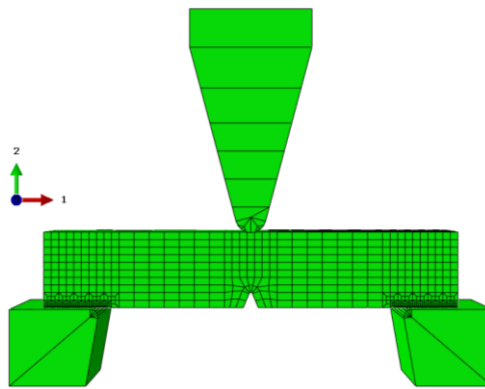
253

254

255 **4. Numerical simulation**

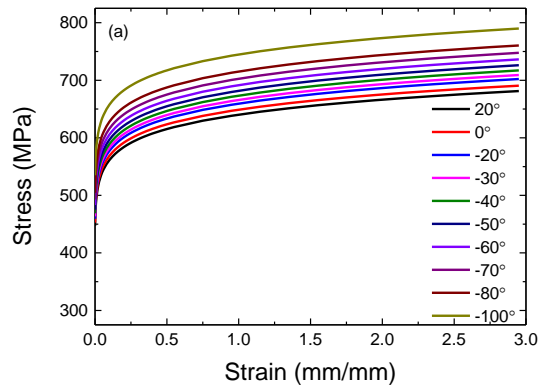
256 An explicit dynamic process is adopted to model the Charpy test by using an explicit code with CAFE
 257 strategy implemented, which has been introduced in Section 2. The geometry of Charpy V-notch
 258 specimen is 55mm*10mm*10mm according to the standard ASTM E23 16b [38], the notch radius
 259 and notch depth are 0.25mm and 2.0mm respectively. The striker and anvils size and geometry are
 260 also those of the standard ASTM E23 16b [38]. The finite element model of Charpy test is shown in
 261 Fig.4, in which the full Charpy specimen is meshed with 8 nodes and reduced integration elements
 262 (C3D8R). Cells are assembled only to those elements in a small region in the center of specimen with
 263 a mesh size around 1mm, so-called damage zone, where damages in a real Charpy specimen is
 264 expected. The striker and two anvils are modelled as elastic body, and are meshed with C3D8R and
 265 C3D6 type of elements. The total number of elements in this model is 8250, in which damage zone
 266 composes of 700 elements. The contact between the Charpy specimen and striker and anvils is
 267 modeled with a friction coefficient 0.15. The initial velocity of striker is 5.5 m/s.

268 It is assumed that L_D and L_B are $200\mu m$ and $100\mu m$ respectively. Then, in the ductile CA arrays,
 269 each cubic array has 5 cells per linear dimension, namely $m_D = 5$. Likewise, in the brittle CA arrays,
 270 each cubic has 10 cells per linear dimension, namely $m_B = 10$. Therefore, in each element or
 271 integration point, there are 125 ductile cells and 1000 brittle cells. Accordingly, the damage zone is
 272 composed of 87500 ductile cells and 700000 brittle cells. It is assumed that the CA array either ductile
 273 or brittle loses the load-bearing capacity when the cells in one orthogonal section of CA array are
 274 failed [21]. Therefore, the maximum numbers of the dead cells in each CA array are taken as
 275 $N_{D-max} = m_D^2 = 25$ for ductile CA array and $N_{B-max} = m_B^2 = 100$ for the brittle CA array. The
 276 concentration factor for ductile CA, e.g., C_D , is 1.4 and that for brittle CA, e.g., C_B , is 1.4 and 11.0
 277 respectively [20].



278
 279 Fig.4 Finite element model of the Charpy test.
 280

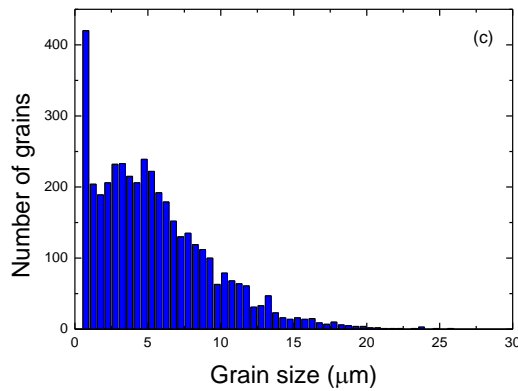
281 The initial void volume fraction f_0 is assumed to be 0.0001. The statistical feature of damage failure
 282 value β_F conforms to a normal distribution, in which the mean value β_{F-mean} is 8.0 and the standard
 283 deviation β_{F-std} is 1.2. The material constant D and σ_1 are 1.65 and 400MPa respectively. These
 284 values of ductile damage variables used in the present work has been calibrated with experimental
 285 results of pure ductile fracture, for example the upper shelf energy (USE) of Charpy test. The flow
 286 property of the TMCR steel at different temperature is presented in Fig.5 (a). The microstructure of
 287 this TMCR steel is presented in the Fig.5 (b), which consists mainly of ferrite and some banded
 288 pearlites. Based on the measurement of grain size of this TMCR steel, the histogram of grain size
 289 distribution is obtained as shown in the Fig.5 (c), which presents a bimodal distribution. Since these
 290 tiny grains will never fracture as they have very high fracture strength, the modelling results are not
 291 affected by omitting this small volume of tiny grains. Hence, an equivalent unimodal three-parameter
 292 Weibull distribution is applied to characterize the grain size distribution of this material, in which the
 293 scale, shape and location parameter are 1.223, 5.392 and 0.516 respectively. The fraction of brittle CA
 294 cells that cleavage is nucleated, η , is assumed to be 0.01, which has been adopted by Shterenlikht et al
 295 [20] as well. The misorientation threshold θ_{th} is assumed to be 40° . The effective surface energy for
 296 the fracture stress of cleavage will be calculated in the section 5.



297



298



299

300 *Fig. 5 The properties and microstructure of TMCr steel: (a) flow stress and strain curve at different*
 301 *test temperatures[21], (b) the microstructure of TMCr steel [20] and (c) the histogram of grain size*
 302 *distribution [20].*

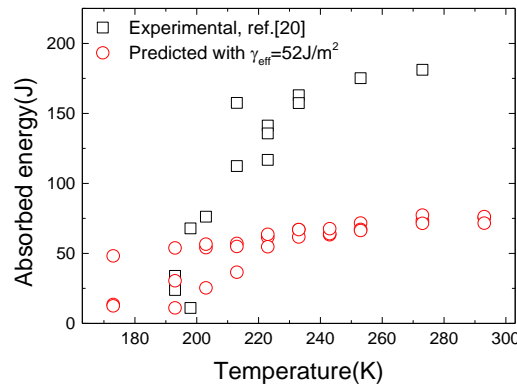
303

304

305 **5. Numerical results and discussion**

306 In the following, we firstly present the predicted results of DBT by using a constant effective surface
 307 energy. To reproduce the transition by using the CAFE method, another temperature dependent
 308 variable, e.g., the temperature dependent effective surface energy, is calculated via the continuum
 309 approach introduced in the Section 3. Although being improved, the DBT predicted with the
 310 calculated temperature dependent effective surface energy indicates that the role of grain boundary in
 311 the cleavage propagation in the transition region cannot be neglected. As such, the lower limit of

312 effective surface energy for overcoming the barrier of grain boundary in the transition region is
 313 estimated based on both the temperature dependent effective surface energy for unstable cleavage
 314 formation and the size ratio of cleavage facet (unit) to critical particle. In the end, an accurate
 315 prediction of DBT of TMCR steel is achieved by using the lower limit of effective surface energy for
 316 crack propagating across the grain boundary.



317

318 *Fig.6 absorbed energy of Charpy impact test in the transition region predicted by CAFE model with a*
 319 *constant effective surface energy, e.g., $\gamma_{eff} = 52 J/m^2$.*

320

321 5.1 DBT prediction by using a constant effective surface energy

322 Firstly, a constant value of the effective surface energy γ_{eff} , $52 J/m^2$, which has been adopted in the
 323 study on the DBT of TMCR steel by Wu et al [23] and Shterenlikht et al [20], is used in the CAFE
 324 model to calculate the fracture stress of cleavage according to equation (3). The other parameters to
 325 model the DBT of TMCR steel have been introduced in the Section 4. The absorbed energy of
 326 standard Charpy tests in the transition region vs. temperature is plotted in the Fig.6, in which the
 327 predicted results by CAFE method with constant effective surface energy compare with the
 328 experimental results by Shterenlikht et al [20]. At each temperature, three runs have been performed.
 329 Since the statistical nature of material has been incorporated in the model, results present a scattered
 330 feature as shown in the Fig.6. It can be found that the predicted absorbed energy at higher temperature
 331 is not as scattered as that at lower temperature since the fewer cleavage happens at higher temperature.
 332 The predicted absorbed energy at lower temperature, e.g., 193K, is comparable to the experimental
 333 results. However, the predicted absorbed energy is dramatically underestimated comparing to the
 334 experimental results. It implies that only temperature-dependent flow stress of material shown in Fig.5
 335 (a) is not adequate to obtain an ideal DBT behavior, which has been similarly reported by Rossoll et al
 336 [16], Tanguy et al [18] and Shterenlikht et al [20]. Thus, the second temperature-dependent parameter
 337 has to be searched so as to accurately represent the DBT behavior of materials.

338

339 5.2 The effective surface energy of TMCR steel

340 5.2.1 Identification of the parameters

341 It is found that the variation of activation energy of DBT among single-crystal iron, poly-crystal iron
 342 and Fe-alloys is relatively minor [39, 40], e.g., in the range of 0.2-0.5. This implies that the minor
 343 difference between parameters calibrated from the activation energies of DBT of different steels can
 344 be expected. In addition, there are still some resemblances between low carbon steel studied by
 345 Tanaka et al [40] and the TMCR steel investigated in the present work, e.g., the ferritic type of
 346 microstructure and controlled-rolling process of production. Since the absence of the test results of
 347 activation energy of DBT of the TMCR steel, a low carbon steel experimentally obtained by Tanaka
 348 et al [40] is utilized to approximately identify the parameters for the calculation of effective surface
 349 energy of the TMCR steel. In the aim of exploring a solution to estimate the effective surface energy
 350 in transition region, the gap between two materials, e.g., low carbon steel and the TMCR steel can be
 351 ignored.

352 As reported in the literature, a relation between loading rate \dot{K} and Θ_c has been found through
 353 experiments [41]

$$\ln \dot{K} = -E_a/k_B \Theta_c + const. \quad (9)$$

354 where E_a is the activation energy for the DBT, which equals to the activation energy Q for dislocation
 355 velocity; Θ_c is critical DBT temperature at which ductile fracture changes to be brittle fracture [33, 35,
 356 36]. Based on the theory of shielding effect of dislocation mobility on crack tip, equation (9) has also
 357 been used to depict the correlation of loading rate and Θ_c of low carbon steel by Tanaka et al [40].
 358 The critical transition temperatures of low carbon steel have been measured through four point
 359 bending tests under different outer-fiber strain rates by Tanaka et al [40]. The outer-fiber strain rate
 360 can be calculated by [42]

$$\dot{\epsilon}_f = \frac{4B}{S_1^2} \dot{\delta} \quad (10)$$

361 where $\dot{\epsilon}_f$ is the outer-fiber strain rate and $\dot{\delta}$ is the cross head speed, B is the thickness of specimen and
 362 S_1 is the outer span of specimen. The applied stress intensity factor of four point bending test can be
 363 calculated by using the equation [43]

$$K_I = \frac{3F(S_1 - S_2)}{2BW^2} \sqrt{a} Y \quad (11)$$

364 where $Y = \frac{1.1215\sqrt{\pi}}{(1-a/W)^{3/2}} \left[\frac{5}{8} - \frac{5}{12} \frac{a}{W} + \frac{1}{8} \left(\frac{a}{W} \right)^2 + 5 \left(\frac{a}{W} \right)^2 \left(1 - \frac{a}{W} \right)^6 + \frac{3}{8} \exp \left(-6.1342 \frac{a}{W-a} \right) \right]$, F is loading
 365 force, S_2 is inner span, W is width of specimen and a is notch depth. To obtain the loading rate of
 366 four point bending test, three-dimensional analysis with a quasi-static process is carried out in the
 367 present study. The cross head speed applied for modelling is converted from outer-fiber strain rates
 368 used by Tanaka et al. [40] in terms of the equation (10). It has to be mentioned that only a stationary

369 crack is studied. The Young's modulus E and poisson's ratio ν of steel are 206 GPa and 0.29
 370 respectively. The loading rate, e.g., the rates of stress intensity factor, applied on the four-point
 371 bending specimen is calculated by equation (11). The outer-fiber strain rates and calculated loading
 372 rate, e.g., the applied rates of stress intensity factor are listed in table 1.

373 Tab.1 The outer-fiber strain rates of the four point bend tests on fully annealed low carbon steel [43]
 374 and the calculated applied rates of stress intensity factor.

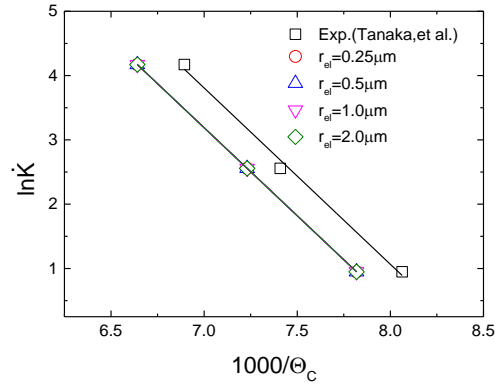
$\dot{\epsilon}(s^{-1})$	$\dot{K}_I^a(MPam^{0.5}s^{-1})$
4.46e-4	2.5790
2.23e-4	12.897
1.12e-2	64.774

375

376 The critical DBT temperature under a specific loading rate can be predicted by using the continuum
 377 approach introduced in section 3. Different elastic zone size (e.g., particle size) of the model is also
 378 studied. To obtain the critical DBT temperatures under the loading rates listed in table 1, for each
 379 elastic zone size, several groups of parameters have been tried following the method introduced
 380 previously by the authors [33]. By doing this, groups of parameters are optimized for each elastic
 381 zone size, which are listed in the table 2. The computed DBT temperatures under different loading
 382 rates are compared with experimental results by Tanaka et al [40] in Fig.7. It is shown that the
 383 computational results of low carbon steel agree well with experimental results, which indicates that
 384 the group of parameters for each elastic zone size is reliable. Meanwhile, the influence of the elastic
 385 zone size on the fracture toughness in the transition region is also studied under the loading rate 10
 386 $MPam^{0.5}s^{-1}$. The applied stress intensity factor K_I^a normalized with the critical stress intensity factor
 387 K_{IC} vs. temperature are plotted in the Fig.8 for each elastic zone size. Here, $K_{IC} = 1.77MPam^{0.5}$ is
 388 calculated from the widely used effective surface energy for cleavage of steel, e.g., $7J/m^2$, tested by
 389 Bowen et al [44] according to Griffith theory. It is shown in Fig.8 that to achieve an identical DBT
 390 temperature Θ_c the minor difference among the fracture toughness for different elastic zone sizes is
 391 presented in the whole temperature range by using the parameters identified above. Recall the
 392 equation (5)-(7), at a specific temperature and under same stress level, when activation energy Q is
 393 determined, with the combination of parameter of $\dot{\epsilon}_0$ and m , the similar amount of shielding effect of
 394 dislocation dynamics and DBT behavior can be always achieved no matter how large the elastic zone
 395 size (particle size) is. To this end, it can be concluded that the predicted DBT of low carbon steel by
 396 using the continuum model is elastic zone size independent. In the later simulation, the parameters
 397 verified for elastic zone size $1\ \mu m$ will be adopted.

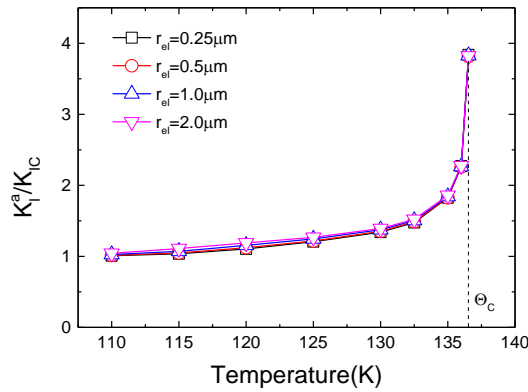
398 Tab.2 Parameters for different elastic zone size.

$r_{el}(\mu m)$	$\dot{\epsilon}_0(s^{-1})$	$Q(ev)$	m	σ_0
0.25	29934.39	0.236	1.45	1.0
0.50	11307.01	0.236	1.70	1.0
1.0	3898.48	0.236	2.00	1.0
2.0	1717.67	0.236	2.30	1.0



399

400 *Fig.7 comparison of computed and experimental critical DBT temperature of low-carbon steel.*



401

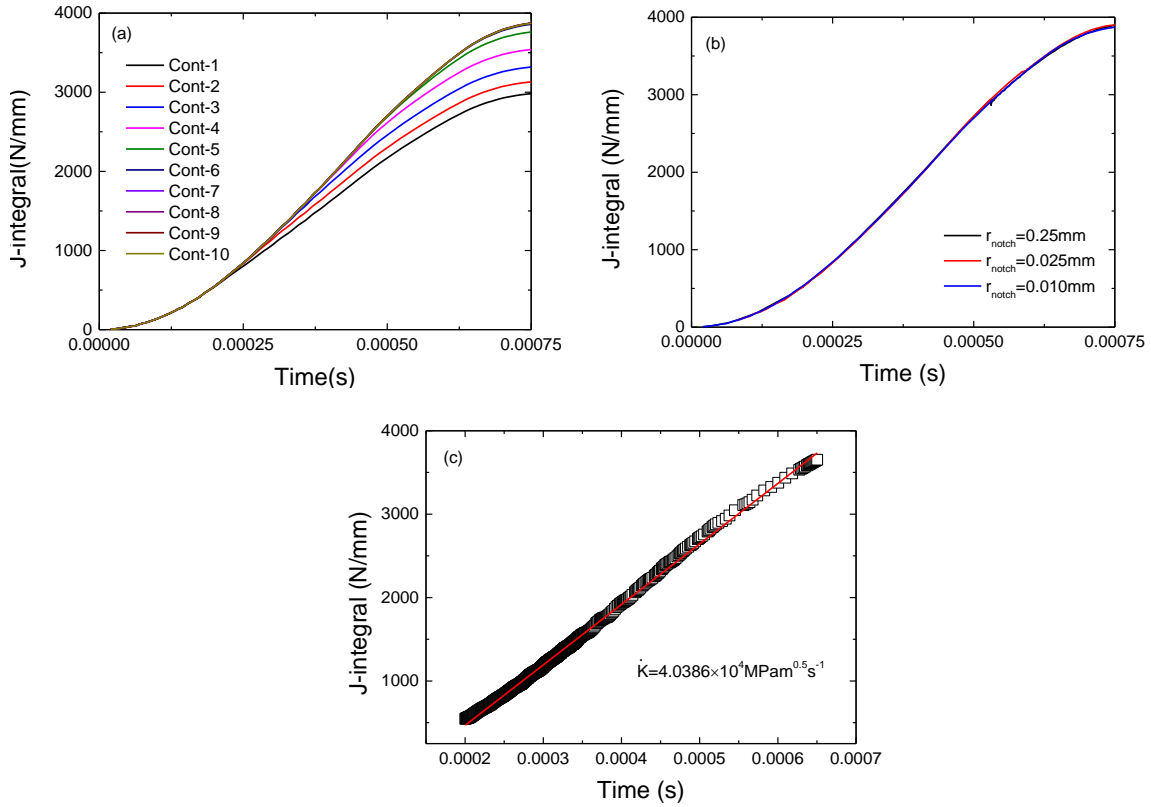
402 *Fig.8 the DBT curve of steel predicted by the continuum model with different elastic zone size. The*
403 *loading rate is $10 MPam^{0.5}s^{-1}$.*

404

405 5.2.2 The temperature dependent effective surface energy

406 As mentioned above, the shielding effect of dislocation mobility on crack tip is loading rate dependent.
407 To obtain the loading rate of Charpy impact test, the three-dimensional analysis of Charpy test is
408 conducted. The geometry of Charpy V-notch specimen is identical to that introduced in the section 4.
409 To model the transient process of impact and obtain the J-integral from Abaqus, a dynamic implicit
410 process is utilized. However, only a stationary crack is studied here. The V-notch Charpy impact
411 specimen is actually replaced by U-notch specimen in the calculation of J-integral since that the
412 identical J-integrals calculated by Abaqus have been obtained from both notch-type specimen with
413 same radius in present study. A path-independence pattern is presented in the Fig.9 (a) in a relative far
414 field (beyond the 5 contours) near notch root. A notch radius independence of J-integrals is presented

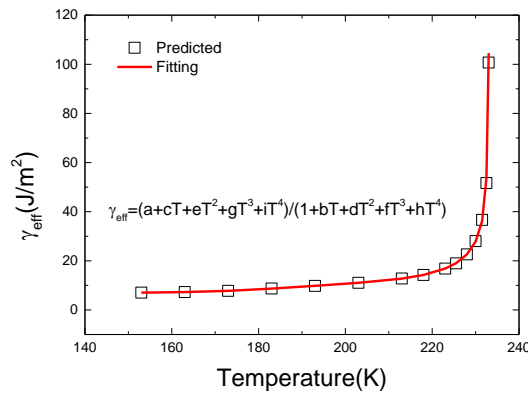
415 in Fig.9 (b). The loading rate \dot{K} of Charpy impact test, $4.0386 \times 10^4 \text{MPam}^{0.5} \text{s}^{-1}$, is achieved by fitting
 416 the linear part of the curve of J-integral vs. time as shown in Fig.9 (c).



417

418

419 *Fig.9 Charpy impact test modelling results: (a) path-independence of J-integral of U-notch specimen*
 420 *with notch radius 0.25mm, (b) J-integral of Charpy impact tests with different notch radius, (c) the*
 421 *loading rate of Charpy impact test. Here, r_{notch} is the notch radius of Charpy specimen.*



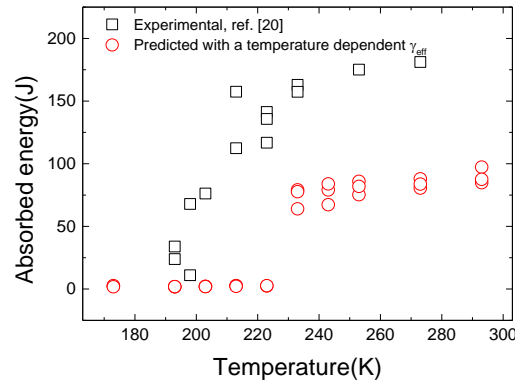
422

423 *Fig.10 the calculated effective surface energy in the transition region by using continuum model,*
 424 *where a, b, c, d, e, f, g, h, i are constant.*

425

426 By applying continuum approach shown in Section 3, the fracture toughness of the TMCR steel in the
 427 DBT region is calculated with parameters identified in section 5.2.1 and the loading rate of Charpy
 428 impact test calculated above. According to equation (8), the effective surface energy of TMCR steel in

429 the transition region is calculated as shown in Fig.10. It can be found that the effective surface energy
 430 of steel in the lower temperature, e.g. below 200K, is very stable and comparatively low. However, it
 431 increase rapidly until the critical DBT temperature when temperature beyond 220K. In addition, an
 432 equation for describing the correlation between the effective surface energy and temperature is
 433 obtained by fitting the calculated effective surface energy at different temperature, see Fig.10. This
 434 equation for temperature dependent effective surface energy will be adopted in the later simulation of
 435 DBT of TMCR steel.



436
 437 *Fig.11 absorbed energy of Charpy impact test in the transition region predicted by CAFE model with*
 438 *a temperature-dependent effective surface energy.*

439
 440 **5.3 DBT of TMCR steel modeled with an effective surface energy**

441 A temperature-dependent effective surface energy law obtained in Section 5.2 (see Fig.10) is applied
 442 to the CAFE method to simulate the DBT of TMCR steel. Here, the procedure and parameters used
 443 for the modelling are identical to those utilized in the Section 5.1 except that a constant value of the
 444 effective surface energy is replaced by the temperature-dependent effective surface energy. The
 445 predicted absorbed Charpy energy vs. temperature is plotted in the Fig.11, in which the experimental
 446 results are also presented for comparison. It can be observed that the DBT transition happens in a very
 447 narrow temperature range and a dramatic steep transition are obtained comparing with the
 448 experimental results. In addition, both lower shelf and upper shelf of DBT are obviously
 449 underestimated.

450 In the process of the unstable cleavage propagation of steel, the second step is critical in terms of the
 451 formation of unstable fracture [45], otherwise the crack stops or be blunted at the interface, and then
 452 the cracked particle may act as the nuclei for void growth when ductile fracture intervenes. The
 453 critical fracture stress for the crack propagation across the interface between the particle and matrix,
 454 e.g., particle cleavage strength σ_{pm} [46], can be calculated by

$$\sigma_{pm} = \left(\frac{\pi E \gamma_{pm}}{(1 - \nu^2)c} \right)^{1/2} \quad (12)$$

455 where γ_{pm} is the effective surface energy to propagate the micro-crack across particle-matrix interface;
 456 c is the particle size. Once unstable fracture formatted, e.g., micro-crack initiation from the particle
 457 and penetration into the matrix, the first grain boundary could be the barrier for unstable cleavage
 458 crack to trespass, see Fig.3 (a).The critical fractures stress, e.g. grain strength σ_{mm} [46], becomes a
 459 criterion for the extension of the crack across the grain boundary, which can be described as

$$\sigma_{mm} = \left(\frac{\pi E \gamma_{mm}}{(1 - \nu^2) d} \right)^{1/2} \quad (13)$$

460 where γ_{mm} is the effective surface energy for crack propagation across the grain boundary; d is grain
 461 size. Comparing with the equation (14), it indicates that

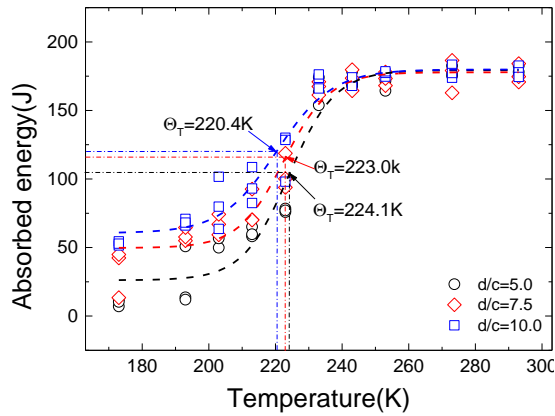
$$\frac{\sigma_{mm}}{\sigma_{pm}} = \frac{\gamma_{mm} c}{\gamma_{pm} d} \quad (14)$$

462 When the local stress near the particle $\sigma_L = \sigma_{mm} < \sigma_{pm}$, the micro-crack could propagate across the
 463 grain boundary, and unstable cleavage fracture would be ensured by the particle cracking. It implies
 464 that the unstable fracture is dominated by the particle size, e.g., cleavage at the lower shelf, where the
 465 local stress near the particle is high enough due to the higher yield stress. However, when $\sigma_L =$
 466 $\sigma_{mm} > \sigma_{pm}$, the crack arrests at the grain boundary, resulting in the appearance of stable and grain-
 467 sized micro-crack. It means that the propagation of unstable fracture is dominated by the grain size,
 468 e.g., cleavage occurring in the transition region, where the local stress near the particle is not adequate
 469 to overcome the grain strength. Therefore, it can be concluded that the role of grain boundary on the
 470 unstable cleavage propagation should not be neglected, and that the cleavage propagation in the
 471 transition region depends on the competition between σ_{mm} and σ_{pm} , e.g., particle dominated or grain
 472 size dominated [46-50].

473 A critical condition for crack propagating across the first grain boundary can be deduced from the
 474 equation (14) when σ_{mm} equals to σ_{pm} , from which the lower limit of the effective surface energy for
 475 crack extension across the grain boundary can be achieved

$$\gamma_{mm} = \gamma_{pm} \frac{d}{c} \quad (15)$$

476 It implies that the minimum of γ_{mm} is solely related the size ratio of grain and particle when the
 477 effective surface energy of cleavage formation of the material, e.g., γ_{pm} , has been obtained. As such,
 478 the γ_{pm} can be transferred to γ_{mm} , by using equation (15). Recall the equation (3), the γ_{mm} is exactly
 479 required to calculate the fracture stress of cleavage in CAFE model. While, the effective surface
 480 energy obtained in the section 5.2, it is actually not the γ_{mm} but the γ_{pm} , which is the reason why the
 481 absorbed energies in the full temperature range is underestimated as shown in the Fig.11.



482

483 *Fig.12 the predicted DBT of TMCR steel with different ratios of d/c . Here, data is fitted by the*
 484 *sigmoidal method. The transition temperature Θ_T is defined as the temperature corresponding to the*
 485 *impact energy halfway between the lower shelf energy (LSE) and USE [49].*

486

487 Based on the γ_{pm} obtained in Section 5.2, DBT of the TMCR steel is predicted with the variable ratio
 488 of d/c as shown in the Fig.12. It can be observed that different ratio of d/c can achieve a similar
 489 upper shelf, while the lower shelf and the absorbed energy in transition region are quite different.
 490 Since complete ductile fracture happens on the upper shelf, the ratio of d/c presents no effect on the
 491 absorbed energy, which is usually only relevant to the cleavage fracture. It is also found that the larger
 492 ratio of d/c enables a higher absorbed energy of steel in the temperature range below the upper shelf.
 493 Meanwhile, a lower transition temperature, Θ_T , is achieved for the larger ratio of d/c . San Martin et
 494 al. [47] has studied the cleavage fracture in the transition region of Ti-V alloyed steel, in which some
 495 isolated cleavage islands could be formed surrounded by ductile fracture. They have measured the
 496 sizes of cleavage islands, e.g., d_{CL} and the sizes of cleavage initiators, e.g. c_{crit} . The effective surface
 497 energy γ_{mm} has been calculated by using a similar transferring rule (e.g., equation (15)), in which the
 498 effective surface energy $\gamma_{pm} = 7 \text{ J/m}^2$ has been adopted. It has been found that the γ_{mm} lineally
 499 increases with the ratio of d_{CL}/c_{crit} . measured at all temperatures in DBT regime. This proves that the
 500 ratio d/c in equation (15) can physically reflect the toughness of material as shown in Fig.12.

501 It is well known that the particle precipitated in the steel is non-uniformly distributed for both size and
 502 spacing. Ahead of the crack/notch tip, the particle is sampled as the cleavage nucleate once the
 503 maximum principle stress ahead of the crack/notch tip is higher than σ_{pm} , see equation (12). However,
 504 the stress ahead of the crack/notch tip generally decreases with the temperature, which means that
 505 accordingly the size of qualified particle to be sampled as the initiator of cleavage decreases with the
 506 decrease of temperature. A linear relation between temperature and critical particle size has been
 507 found in SA 508 steel by Lee et al [51]. Since the grain size is temperature independent, it implies
 508 that the ratio of d/c is not a constant value in the transition regime but a variable relevant to the

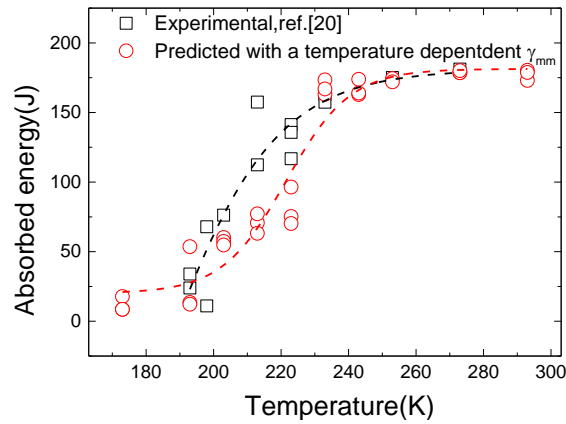
509 temperature. In addition, the crystallographic unit of cleavage could not be the grain size, since crack
 510 deflection or arrest usually does not happens at the lower grain boundary. Whilst, it has been pointed
 511 out that the cleavage fracture unit (facet) size or the effective grain size is more suitable to describe
 512 the cleavage fracture unit, and that both of them match each other very well in Mn-Mo-Ni low alloy
 513 steel [52]. To accurately describe the competition between σ_{pm} and σ_{mm} of cleavage fracture in the
 514 transition region, the grain size d in equation (15) should be modified to the cleavage facet (unit) size
 515 $d_{CF(U)S}$ or effective grain size d_{EGS} . According to the findings by Lee et al [51], a linear relation
 516 between the ratio of $d_{CF(U)S}/c_{crit.}$ or $d_{EGS}/c_{crit.}$ and temperature could be expected since that the
 517 $d_{CF(U)S}$ is generally temperature independent. To this end, a linear correlation between $d_{CF(U)S}/c_{crit.}$
 518 and temperature is assumed

$$\frac{d_{CF(U)S}}{c_{crit.}} = -0.025(\Theta - 273) + 4.0 \quad (16)$$

519 where Θ is temperature. Then, the effective surface energy obtained in section 5.2 as shown in Fig.10
 520 is corrected by the ratio of $d_{CF(U)S}/c_{crit.}$ in equation (16) according to the equation (15), from which
 521 the γ_{mm} can be obtained. Then, the calculated γ_{mm} is implemented in CAFE model to predict the
 522 DBT of TMCR steel. The predicted absorbed energy vs. temperature is plotted in the Fig.13, in which
 523 the experimental results of TMCR steel is also presented for comparison. It is observed that
 524 simulation is able to produce a full transition curve with a scatter pattern of absorbed energies in the
 525 transition region. Generally, the predicted transition curve is comparative to the experimental results.
 526 The simulation can reproduce a similar LSE and USE comparing with the experimental results, while
 527 the absorbed energy in transition region is slightly underestimated comparing with the experimental
 528 results.

529 It is not surprising for the underestimation of the absorbed energy in the transition region as shown in
 530 Fig.13 because that the γ_{mm} estimated from equation (15) is just its lower limit. Actually, it is very
 531 difficult to precisely measure or predict the effective surface energy for crack propagating across the
 532 grain boundary [47, 50]. In the section 5.2, a constant exponent m that describes the correlation
 533 between dislocation velocity and resolved shear stress is used to estimate the effective surface energy
 534 of unstable cleavage formation (e.g., the second step) in the transition region, see equation (6) and (7).
 535 However, it has been found that m decreases with the increase of temperature [53, 54], which means
 536 that the fracture toughness in transition region could be underestimated since the lower m can lead to a
 537 higher toughness [35] in the transition region. Accordingly, the γ_{pm} for cleavage penetration into
 538 matrix could be under-predicted as well. This could be a reason why the predicted absorbed energies
 539 in the transition region are lower than those of experimental results as shown in Fig.13. Since the
 540 lacking of the experimental correlation between the ratio of $d_{CF(U)S}/c_{crit.}$ and temperature for this
 541 TMCR steel, an artificial linear relation between them is assumed to transfer the γ_{pm} to γ_{mm} , which is

542 inspired by the study in ref. [51]. Therefore, measurements on the critical particle size and the
 543 cleavage facet (unit) size of steel have to be conducted so as to find a more reliable temperature
 544 dependent ratio of $d_{CF(U)S}/c_{crit}$.



545
 546 *Fig.13 absorbed energy of Charpy impact test in the transition region predicted by CAFE model with*
 547 *a temperature-dependent effective surface energy corrected by a temperature dependent ratio of*
 548 *$d_{CF(U)S}/c_{crit}$. Here, data is fitted by the sigmoidal method.*

549
 550

551 **6. Conclusions**

552 In this study the CAFE method developed by Shterenlikht et al [20-22] has been applied to mitigate
 553 some of the computational challenges in modelling of DBT and incorporate the statistical nature of
 554 microstructure at the same time. In order to realistically capture the temperature dependent fracture
 555 toughness in the transition region, a physical based variable has to be searched, which is also one of
 556 the motivations of this work. On the basis of our previous work [33] a continuum approach has been
 557 developed to estimate the effective surface energy for unstable cleavage formation, e.g., γ_{pm} . Further,
 558 to describe the essence of the competition between particle size and grain size-controlled propagation
 559 of unstable cleavage, a more robust variable, effective surface energy for overcoming the barrier of
 560 grain boundary, e.g., γ_{mm} , was proposed. Finally, a framework for the modelling of DBT is explored
 561 through implementing the γ_{mm} into the CAFE method. Some important findings obtained in present
 562 work can be summarized as followings:

- 563 • It is proved that a second temperature dependent variable has to be found to reproduce the
 564 DBT curve, in addition to the temperature dependent flow properties. In present work, a
 565 continuum approach has been developed to establish the second temperature dependent
 566 variable, e.g., γ_{pm} .

- 567 • It is observed that the role of grain boundary on the unstable cleavage propagation cannot be
568 ignored. Through analyzing the competition between the particle size and grain size
569 dominated unstable cleavage propagation, a method to quantify the lower limit of γ_{mm} has
570 been built.
- 571 • Due to the fact that cleavage facet (unit) size or effective grain size, e.g., $d_{CF(U)S}$, rather than
572 the grain size is more appropriate for characterizing the cleavage fracture unit, the ratio of
573 grain size to critical particle size has been replaced by $d_{CF(U)S}/c_{crit.}$ in the estimation of γ_{mm} .
- 574 • It is found that numerical simulation by using the CAFE method implemented with γ_{mm} is
575 able to produce a full transition curve, especially with scattered absorbed energies in the
576 transition region represented.

577 Although a framework of modelling DBT of steel is explored in this work, it still has some limitations.
578 More experimental results are required for the calibration of parameters to calculate the temperature
579 effective surface energy adopted in present work, for instance, the activation energy for the DBT and
580 the temperature dependent ratio of $d_{CF(U)S}/c_{crit.}$ of the TMCR steel. In addition, the adiabatic heating
581 effect and viscoplastic of material is not considered in Charpy impact modelling.

582

583

584 *Acknowledgements*

585 The authors wish to thank the Research Council of Norway for funding through the Petromaks 2
586 Programme, Contract No.228513/E30. The financial support from Eni, Statoil, Lundin, Total, JFE
587 Steel Corporation, Posco, Kobe Steel, SSAB, Bredero Shaw, Borealis, Trelleborg, Nexans, Aker
588 Solutions, FMC Kongsberg Subsea, Kværner Verdal, Marine Aluminium, Hydro and Sapa are also
589 acknowledged.

590

591

592 **References**

- 593 [1] A.L. Gurson, Continuum Theory of Ductile Rupture by Void Nucleation and Growth: Part I—
594 Yield Criteria and Flow Rules for Porous Ductile Media, *Journal of Engineering Materials and*
595 *Technology* 99(1) (1977) 2-15.
- 596 [2] V. Tvergaard, A. Needleman, Analysis of the cup-cone fracture in a round tensile bar, *Acta*
597 *Metallurgica* 32(1) (1984) 157-169.
- 598 [3] Z.L. Zhang, C. Thaulow, J. Ødegård, A complete Gurson model approach for ductile fracture,
599 *Engineering Fracture Mechanics* 67(2) (2000) 155-168.
- 600 [4] T. Pardoen, J.W. Hutchinson, An extended model for void growth and coalescence, *Journal of the*
601 *Mechanics and Physics of Solids* 48(12) (2000) 2467-2512.
- 602 [5] G. Rousselier, Ductile fracture models and their potential in local approach of fracture, *Nuclear*
603 *Engineering and Design* 105(1) (1987) 97-111.

604 [6] A. Pineau, A.A. Benzerga, T. Pardoen, Failure of metals I: Brittle and ductile fracture, *Acta*
605 *Materialia* 107 (2016) 424-483.

606 [7] R.O. Ritchie, J.F. Knott, J.R. Rice, On the relationship between critical tensile stress and fracture
607 toughness in mild steel, *Journal of the Mechanics and Physics of Solids* 21(6) (1973) 395-410.

608 [8] F.M. Beremin, A. Pineau, F. Mudry, J.-C. Devaux, Y. D'Escatha, P. Ledermann, A local criterion
609 for cleavage fracture of a nuclear pressure vessel steel, *Metallurgical Transactions A* 14(11) (1983)
610 2277-2287.

611 [9] T. Lin, A.G. Evans, R.O. Ritchie, A statistical model of brittle fracture by transgranular cleavage,
612 *Journal of the Mechanics and Physics of Solids* 34(5) (1986) 477-497.

613 [10] K. Wallin, T. Saario, K. Törrönen, Statistical model for carbide induced brittle fracture in steel,
614 *Metal Science* 18(1) (1984) 13-16.

615 [11] M.K. Samal, M. Seidenfuss, E. Roos, B.K. Dutta, H.S. Kushwaha, Experimental and numerical
616 investigation of ductile-to-brittle transition in a pressure vessel steel, *Materials Science and*
617 *Engineering: A* 496(1) (2008) 25-35.

618 [12] M.K. Samal, J.K. Chakravarty, M. Seidenfuss, E. Roos, Evaluation of fracture toughness and its
619 scatter in the DBTT region of different types of pressure vessel steels, *Engineering Failure Analysis*
620 18(1) (2011) 172-185.

621 [13] V. Tvergaard, A. Needleman, An analysis of the temperature and rate dependence of Charpy V-
622 notch energies for a high nitrogen steel, *International Journal of Fracture* 37(3) (1988) 197-215.

623 [14] V. Tvergaard, A. Needleman, An analysis of the brittle-ductile transition in dynamic crack
624 growth, *International Journal of Fracture* 59(1) (1993) 53-67.

625 [15] A. Needleman, V. Tvergaard, Numerical modeling of the ductile-brittle transition, *International*
626 *Journal of Fracture* 101(1) (2000) 73.

627 [16] A. Rossoll, C. Berdin, C. Prioul, Determination of the Fracture Toughness of a Low Alloy Steel
628 by the Instrumented Charpy Impact Test, *International Journal of Fracture* 115(3) (2002) 205-226.

629 [17] B. Tanguy, J. Besson, R. Piques, A. Pineau, Ductile to brittle transition of an A508 steel
630 characterized by Charpy impact test: Part I: experimental results, *Engineering Fracture Mechanics*
631 72(1) (2005) 49-72.

632 [18] B. Tanguy, J. Besson, R. Piques, A. Pineau, Ductile to brittle transition of an A508 steel
633 characterized by Charpy impact test: Part II: modeling of the Charpy transition curve, *Engineering*
634 *Fracture Mechanics* 72(3) (2005) 413-434.

635 [19] G. Hütter, T. Linse, S. Roth, U. Mühlich, M. Kuna, A modeling approach for the complete
636 ductile–brittle transition region: cohesive zone in combination with a non-local Gurson-model,
637 *International Journal of Fracture* 185(1) (2014) 129-153.

638 [20] A. Shterenlikht, I.C. Howard, The CAFE model of fracture—application to a TMCR steel,
639 *Fatigue & Fracture of Engineering Materials & Structures* 29(9-10) (2006) 770-787.

640 [21] A. Shterenlikht, 3D CAFE modelling of transitional ductile-brittle fracture in steel, The
641 University of Sheffield, UK, 2003.

642 [22] A. Shterenlikht, I.C. Howard, Cellular Automata Finite Element (CAFE) modelling of
643 transitional ductile-brittle fracture in steel, The 15th European Conference of Fracture (ECF15), KTH,
644 Stockholm, Sweden, 2004.

645 [23] S.J. Wu, C.L. Davis, A. Shterenlikht, I.C. Howard, Modeling the ductile-brittle transition
646 behavior in thermomechanically controlled rolled steels, *Metall and Mat Trans A* 36(4) (2005) 989-
647 997.

648 [24] S. Das, A. Shterenlikht, I.C. Howard, E.J. Palmiere, A general method for coupling
649 microstructural response with structural performance, *Proceedings of the Royal Society A:*
650 *Mathematical, Physical and Engineering Science* 462(2071) (2006) 2085-2096.

651 [25] A. Shterenlikht, L. Margetts, Three-dimensional cellular automata modelling of cleavage
652 propagation across crystal boundaries in polycrystalline microstructures, *Proceedings of the Royal*
653 *Society of London A: Mathematical, Physical and Engineering Sciences* 471(2177) (2015).

654 [26] Standard Test Method for Determination of Reference Temperature, T_0 , for Ferritic Steels in the
655 Transition Range (ASTM E1921-18), American Society for Testing and Materials, 2018.

656 [27] J.P. Petti, R.H. Dodds, Calibration of the Weibull stress scale parameter, σ_u , using the Master
657 Curve, *Engineering Fracture Mechanics* 72(1) (2005) 91-120.

658 [28] B. Wasiluk, J.P. Petti, R.H. Dodds, Temperature dependence of Weibull stress parameters:
659 Studies using the Euro-material, *Engineering Fracture Mechanics* 73(8) (2006) 1046-1069.

660 [29] Y. Cao, H. Hui, G. Wang, F.-Z. Xuan, Inferring the temperature dependence of Beremin
661 cleavage model parameters from the Master Curve, *Nuclear Engineering and Design* 241(1) (2011)
662 39-45.

663 [30] G. Qian, V.F. González-Albuixech, M. Niffenegger, Calibration of Beremin model with the
664 Master Curve, *Engineering Fracture Mechanics* 136 (2015) 15-25.

665 [31] X. Gao, G. Zhang, T.S. Srivatsan, A probabilistic model for prediction of cleavage fracture in the
666 ductile-to-brittle transition region and the effect of temperature on model parameters, *Materials*
667 *Science and Engineering: A* 415(1) (2006) 264-272.

668 [32] M. Moattari, I. Sattari-Far, I. Persechino, N. Bonora, Prediction of fracture toughness in ductile-
669 to-brittle transition region using combined CDM and Beremin models, *Materials Science and*
670 *Engineering: A* 657 (2016) 161-172.

671 [33] Y. Li, X. Ren, J. He, Z. Zhang, Constraint effect on the brittle-to-ductile transition of single-
672 crystal iron induced by dislocation mobility, *International Journal of Mechanical Sciences* 149 (2018)
673 212-223.

674 [34] M. Stec, J. Faleskog, Micromechanical modeling of grain boundary resistance to cleavage crack
675 propagation in ferritic steels, *International Journal of Fracture* 160(2) (2009) 151.

676 [35] V.R. Nitzsche, K.J. Hsia, Modelling of dislocation mobility controlled brittle-to-ductile transition,
677 *Materials Science and Engineering: A* 176(1) (1994) 155-164.

678 [36] A. Hartmaier, P. Gumbsch, Thermal activation of crack-tip plasticity: The brittle or ductile
679 response of a stationary crack loaded to failure, *Physical Review B* 71(2) (2005) 024108.

680 [37] A.S. Argon, Mechanics and Physics of Brittle to Ductile Transitions in Fracture, *Journal of*
681 *Engineering Materials and Technology* 123(1) (2000) 1-11.

682 [38] ASTM E23-18 Standard Test Methods for Notched Bar Impact Testing of Metallic Materials,
683 2018.

684 [39] A. Giannattasio, M. Tanaka, T.D. Joseph, S.G. Roberts, An empirical correlation between
685 temperature and activation energy for brittle-to-ductile transitions in single-phase materials, *Physica*
686 *Scripta* 2007(T128) (2007) 87.

687 [40] M. Tanaka, K. Higashida, T. Shimokawa, T. Morikawa, Brittle-Ductile Transition in Low
688 Carbon Steel Deformed by the Accumulative Roll Bonding Process, *MATERIALS*
689 *TRANSACTIONS* 50(1) (2009) 56-63.

690 [41] P.B. Hirsch, S.G. Roberts, The brittle-ductile transition in silicon, *Philosophical Magazine A*
691 64(1) (1991) 55-80.

692 [42] G.W. Hollenberg, G.R. Terwilliger, R.S. Gordon, Calculation of Stresses and Strains in Four-
693 Point Bending Creep Tests, *Journal of the American Ceramic Society* 54(4) (1971) 196-199.

694 [43] T. Fett, Stress Intensity Factors – T-Stresses – Weight Functions, Supplement Volume, KIT
695 Scientific Publishing, 2009.

696 [44] P. Bowen, S.G. Druce, J.F. Knott, Effects of microstructure on cleavage fracture in pressure
697 vessel steel, *Acta Metallurgica* 34(6) (1986) 1121-1131.

698 [45] M. Kroon, J. Faleskog, Micromechanics of cleavage fracture initiation in ferritic steels by carbide
699 cracking, *Journal of the Mechanics and Physics of Solids* 53(1) (2005) 171-196.

700 [46] T. Lin, A.G. Evans, R.O. Ritchie, Stochastic modeling of the independent roles of particle size
701 and grain size in transgranular cleavage fracture, *Metall and Mat Trans A* 18(4) (1987) 641-651.

702 [47] J.I. San Martín, J.M. Rodríguez-Ibabe, Determination of energetic parameters controlling
703 cleavage fracture in a Ti-V microalloyed ferrite-pearlite steel, *Scripta Materialia* 40(4) (1999) 459-464.

704 [48] L. Rancel, M. Gómez, S.F. Medina, I. Gutierrez, Measurement of bainite packet size and its
705 influence on cleavage fracture in a medium carbon bainitic steel, *Materials Science and Engineering:*
706 *A* 530 (2011) 21-27.

707 [49] A. Ghosh, A. Ray, D. Chakrabarti, C.L. Davis, Cleavage initiation in steel: Competition between
708 large grains and large particles, *Materials Science and Engineering: A* 561 (2013) 126-135.

709 [50] M.A. Linaza, J.M. Rodríguez-Ibabe, J.J. Urcola, DETERMINATION OF THE ENERGETIC
710 PARAMETERS CONTROLLING CLEAVAGE FRACTURE INITIATION IN STEELS, *Fatigue &*
711 *Fracture of Engineering Materials & Structures* 20(5) (1997) 619-632.

- 712 [51] S. Lee, S. Kim, B. Hwang, B.S. Lee, C.G. Lee, Effect of carbide distribution on the fracture
713 toughness in the transition temperature region of an SA 508 steel, *Acta Materialia* 50(19) (2002)
714 4755-4762.
- 715 [52] S. Kim, S. Lee, B.S. Lee, Effects of grain size on fracture toughness in transition temperature
716 region of Mn–Mo–Ni low-alloy steels, *Materials Science and Engineering: A* 359(1) (2003) 198-209.
- 717 [53] H.W. Schadler, Mobility of edge dislocations on {110} planes in tungsten single crystals, *Acta*
718 *Metallurgica* 12(8) (1964) 861-870.
- 719 [54] H.A. Khater, D.J. Bacon, Dislocation core structure and dynamics in two atomic models of α -
720 zirconium, *Acta Materialia* 58(8) (2010) 2978-2987.

721